

A SURVEY OF GALAXY KINEMATICS TO $Z \sim 1$ IN THE TKRS/GOODS-N FIELD. II. EVOLUTION IN THE TULLY-FISHER RELATION¹

BENJAMIN J. WEINER², CHRISTOPHER N.A. WILLMER^{3,4}, S.M. FABER⁵, JUSTIN HARKER⁵, SUSAN A. KASSIN⁵, ANDREW C. PHILLIPS⁵, JASON MELBOURNE⁵, A.J. METEVIER^{6,7}, N.P. VOGT⁸, D.C. KOO⁵

Accepted by ApJ

ABSTRACT

We use kinematic measurements of a large sample of galaxies from the Team Keck Redshift Survey in the GOODS-N field to measure evolution in the optical and near-IR Tully-Fisher relations to $z = 1.2$. We construct Tully-Fisher relations with integrated line-of-sight velocity widths of ~ 1000 galaxies in B and ~ 670 in J ; these relations have large scatter, and we derive a maximum-likelihood least squares method for fitting in the presence of scatter. The B -band Tully-Fisher relations, from $z = 0.4$ to $z = 1.2$, show evolution of $\sim 1.0 - 1.5$ mag internal to our sample without requiring calibration to a local TF relation. There is evolution in both Tully-Fisher intercept and slope, suggesting differential luminosity evolution. In J -band, there is evolution in slope but little evolution in overall luminosity. The slope measurements imply that bright, massive blue galaxies fade *more strongly* than fainter blue galaxies from $z \sim 1.2$ to now. This conclusion runs counter to some previous measurements and to our naive expectations, but we present a simple set of star formation histories to show that it arises naturally if massive galaxies have shorter timescales of star formation, forming most of their stars before $z \sim 1$, while less massive galaxies form stars at more slowly declining rates. This model predicts that the higher global star formation rate at $z \sim 1$ is mostly due to higher SFR in massive galaxies. The amount of fading in B constrains star formation timescale more strongly than redshift of formation. Tully-Fisher and color-magnitude relations can provide global constraints on the luminosity evolution and star formation history of blue galaxies.

Subject headings: galaxies: distances and redshifts — galaxies: evolution — galaxies: fundamental parameters — galaxies: high-redshift — galaxies: structure — surveys

1. INTRODUCTION

Surveys of large samples of galaxies at significant look-back times are a powerful instrument for measuring the evolutionary history of galaxies. First steps in these probes include measuring number distributions of galaxies, such as the galaxy luminosity function and color-magnitude distribution. A second step is the measurement of scaling relations of galaxy properties.

Locally, relations between galaxy luminosity and characteristic internal kinematic velocity – the Tully-Fisher (TF) relation for disks, the $D_n - \sigma$ relation for spheroidals and its descendant, the Fundamental Plane – are among the tightest correlations and strongest tools for characterizing galaxies. These relations can be used to probe evolution in galaxy properties, and simultaneously, a successful scenario for galaxy formation and evolution will have to reproduce these relations, their scatter, and their

evolution with cosmic time. However, measuring galaxy internal kinematics at intermediate to high redshift is difficult since the sources are faint and high spectral resolution is needed.

In Paper I (Weiner et al. 2006) we presented measurements of galaxy kinematics from emission lines, using Keck/DEIMOS spectra from the Team Keck Redshift Survey (TKRS) in the GOODS-N (Great Observatories Origins Deep Survey) field (Wirth et al. 2004; Giavalisco et al. 2004). The sample with kinematics from Paper I contains ~ 1000 emission line velocity dispersions from integrated emission, with median $\langle z \rangle = 0.637$, and reaches beyond $z > 1$. We use integrated linewidths for fitting Tully-Fisher relations in restframe B and J bands. For a subsample of 380 galaxies, we fit the 2-d spectra to model spatially resolved rotation and dispersion. Paper I compared the properties of the spatially resolved rotation and dispersion to validate the integrated linewidths.

A number of previous studies have measured luminosity-velocity relations from $0.1 < z < 1.0$. Forbes et al. (1996), Rix et al. (1997) and Mallén-Ornelas et al. (1999) used velocity dispersions from integrated emission for ~ 20 galaxies each at median redshifts 0.48, 0.25 and 0.55. The pioneering studies of Vogt et al. (1996, 1997) modeled rotation curves for 17 galaxies of disk morphology with median $\langle z \rangle = 0.47$ by combining Keck/LRIS slitlet spectra with structural information from HST photometry. Subsequent studies of rotation curves with similar modeling procedures include Simard & Pritchett (1998); Vogt (2000); Ziegler et al. (2002) and Bohm et al. (2004); Milvang-Jensen et al. (2003), Bamford et al. (2005, 2006), and Nakamura et al. (2006);

¹ Based in part on observations taken at the W.M. Keck Observatory, which is operated jointly by the University of California and the California Institute of Technology

² Department of Astronomy, University of Maryland, College Park, MD 20742, bjl@astro.umd.edu. Present address: Steward Observatory, University of Arizona, 933 N. Cherry Av., Tucson, AZ 85721

³ Steward Observatory, University of Arizona, 933 N. Cherry Av., Tucson, AZ 85721

⁴ On leave from Observatorio Nacional, Rio de Janeiro, Brasil

⁵ UCO/Lick Observatory, University of California, Santa Cruz, Santa Cruz, CA 95064

⁶ Center for Adaptive Optics, University of California, Santa Cruz, Santa Cruz, CA 95064

⁷ NSF Astronomy and Astrophysics Postdoctoral Fellow

⁸ Department of Astronomy, New Mexico State University, P. O. Box 30001, Las Cruces, NM 88003

Metevier et al. (2006); and Conselice et al. (2005) who used K -band imaging of galaxies in the HST Groth Strip. These generally contained 20–100 galaxies with median redshifts $\sim 0.4 - 0.5$, and include field and cluster samples.

These studies have produced a range of results for evolution in the zeropoint of the Tully-Fisher relation; we discuss comparisons of TF results in Section 4. TF measurements from resolved rotation curves have mostly indicated a relatively mild amount of magnitude evolution. Previous samples are drawn from a variety of populations and selection criteria. In general, samples for measuring rotation curves have been selected to be inclined disk objects with measurable and reasonably orderly rotation.

By contrast, the sample reported here is essentially selected only on magnitude and emission line strength. The lack of selection may be important, given evidence that peculiar and disturbed galaxies are more common at high redshift (e.g. Abraham et al. 1996). The TKRS sample is also large and spans redshifts from 0.1 to 1.6, which allows a measurement of Tully-Fisher relation evolution internal to the sample rather than by comparison to a fiducial local Tully-Fisher relation. Our primary tool for measuring kinematics is one-dimensional line-of-sight velocity dispersion (linewidth), and secondarily the spatially resolved rotation profiles. Paper I discussed the properties of these velocity measures, and showed that integrated linewidth as a measure of the characteristic velocity of a galaxy is fairly robust against observational effects and the details of galaxy kinematics, and that we can measure velocities even for galaxies that are kinematically anomalous or not in orderly rotation, albeit with scatter due to the geometries of velocity fields and inclinations.

We adopt an LCDM cosmology with $h = 0.7$, $\Omega_M = 0.3$, and $\Omega_\Lambda = 0.7$. Magnitudes quoted in this paper are in the AB system unless explicitly indicated as Vega. The sample and observations are discussed in Paper I; Section 2 briefly introduces the data. Section 3 presents Tully-Fisher relations for integrated linewidths and for rotation curves, and measures their evolution. Section 4 compares to other TF measurements, Section 5 discusses the causes of evolution in TF relation, and Section 6 uses luminosity evolution models to interpret the TF evolution. In the Appendix we derive a maximum likelihood method for fitting relations, such as our Tully-Fisher relation, that have a substantial scatter.

2. THE DATA, TULLY-FISHER SAMPLES, AND KINEMATIC PROPERTIES

2.1. Photometric data and samples for Tully-Fisher

The sample of galaxies used for study of the Tully-Fisher relation in this paper is drawn from the the Team Keck Redshift Survey (TKRS) in the GOODS-N field (With et al. 2004). The properties and completeness of the sample are described at length in Paper I; we summarize key points here.

We construct restframe absolute magnitudes M_B and M_J and restframe colors $U - B$ and $R - J$ from SED fitting to the $BVRI$ and HK' magnitudes of Capak et al. (2004). We use a family of SEDs to determine the mapping from observed colors to K-correction and restframe color at each galaxy’s redshift. The median errors on M_B and M_J are 0.11 and 0.14 mag respectively. All

magnitudes in this paper are on the AB system unless otherwise noted.

For the purpose of fitting Tully-Fisher relations, we exclude the faint end of our galaxy sample. The faintest galaxies are only visible at low redshift, so are less useful for comparisons across a range of redshifts. Additionally, the linearity of our observed Tully-Fisher relation can break down at faint magnitudes and small integrated linewidths. We impose magnitude cuts of $M_B < -18$ and $M_J < -19$, which affect the $z < 0.5$ part of our sample. Additionally, because the spectroscopic sample is selected in apparent R , the magnitude limit is a tilted line in the plane of restframe M_B and $U - B$, and the tilt evolves with redshift. To test for any bias caused by the color-magnitude selection, we also constructed a matched sample by imposing a single color tilt, and a magnitude limit that evolves to track L^* for blue galaxies; this limit is shown as the diagonal lines in Figure 3 of Paper I, and is discussed further in Section 3.2.2.

2.2. Kinematic measures and their properties

Our primary kinematic measure is the line-of-sight dispersion of integrated emission σ_{1d} , measured in the TKRS DEIMOS spectra boxcar extracted to 1-D. DEIMOS has a resolution of $\sigma_{inst} = 1.4 \text{ \AA}$ with the 600 lines/mm grating as used for the TKRS, with $1.0''$ slits. For measuring $[\text{O II}]$ in a galaxy at $z = 1$, the resolution corresponds to $c\sigma_{inst}/\lambda_{obs} = 56 \text{ km s}^{-1}$ in the rest frame. Although the resolution depends on λ_{obs} , because the wavelength range of the spectra is limited and different lines are used at different redshifts, the resolution does not vary grossly with redshift. The observed widths of lines σ_{obs} are measured by fitting Gaussians as described in Paper I, and the intrinsic line-of-sight velocity dispersion is computed from

$$\sigma_{1d} = \frac{c}{\lambda_{obs}} \sqrt{\sigma_{obs}^2 - \sigma_{inst}^2}. \quad (1)$$

The emission line kinematic measure from the dispersion of integrated emission is available for $\sim 90\%$ of galaxies with redshifts on the blue side of the bimodal color distribution, with restframe $U - B < 0.95$, but for very few red galaxies, as discussed in Paper I. For blue galaxies, the success rate for measuring linewidth is not strongly dependent on magnitude or color. However, for galaxies with low intrinsic dispersion $\sigma_{1d} \lesssim c\sigma_{inst}/\lambda_{obs}$, it is difficult to measure σ_{1d} accurately. As discussed in Paper I, it is possible for subtraction in quadrature of σ_{inst} to yield a formally very small or negative intrinsic dispersion σ_{1d} , even though it is not physically realistic. Small σ_{1d} leads to very large error on $\log \sigma_{1d}$. We refer to these galaxies, with observed widths close to or less than instrumental, as “kinematically unresolved,” and define them as meeting the criteria on restframe dispersion error ($\log \sigma_{1d} > 0.25$, $\text{error}(\sigma_{1d}) < 30$, and $\sigma_{1d} < 25 \text{ km s}^{-1}$).

Rejecting these galaxies would lead to a bias by preferentially rejecting low-velocity galaxies, so for plotting and fitting purposes we assign them a low velocity, $\log \sigma_{1d} = 1.4 \pm 0.2$ ($\sigma_{1d} = 25 \text{ km s}^{-1}$). The results of fitting do not depend strongly on the exact value assigned. We do reject galaxies with $\sigma_{1d} > 25 \text{ km s}^{-1}$ and $\text{error}(\log \sigma_{1d}) > 0.25$; for these, the large error is usually

a sign of a bad fit or data contaminated by night sky lines. Including kinematically unresolved galaxies, there are 913 galaxies with acceptable σ_{1d} and $M_B < -18$, and 647 with σ_{1d} and $M_J < -19$. In Section 3.2 we outline a fitting method which treats these unresolved galaxies more robustly by fitting the ensemble of observed width σ_{obs} before the instrumental resolution is subtracted.

For a subset of galaxies selected on size and emission line strength, we also fit a kinematic model to the 2-d spectrum, measuring the spatially resolved kinematics with line-of-sight terminal velocity of the rotation curve V_{rot} , and dispersion σ_{2d} . 380 galaxies yielded good spatially resolved fits. The dispersion σ_{2d} from the spatially resolved fits differs from the dispersion computed from integrated linewidth σ_{1d} because the integrated linewidth also includes the velocity spread caused by the rotation gradient.

The modeling of velocity fields in Section 4 of Paper I shows how the integrated linewidth can represent the velocity spread in the full galaxy velocity field, because the linewidth arises from different velocities mixed together by seeing. In Section 5 of Paper I we also compared the integrated kinematic measure σ_{1d} with the measures from resolved fits, V_{rot} and σ_{2d} , and with combinations of the resolved measures, e.g. $S_{0.5}^2 = 0.5V_{rot}^2 + \sigma_{2d}^2$. We concluded that σ_{1d} correlates well with the combination of the resolved measures, and as a probe of galaxy internal kinematics, is fairly robust against observational effects such as slit position angle, although there is scatter in σ_{1d} due to galaxy properties such as inclination. We found that galaxies with spatially resolved kinematics fall on a range between rotation dominated, $V_{rot}/\sigma_{2d} > 1$, and dispersion dominated, $V_{rot}/\sigma_{2d} < 1$; the 1-d linewidth σ_{1d} and the combined velocity scale $S_{0.5}$ are better proxies for kinematics than either V_{rot} or σ_{2d} alone.

We found that a significant fraction of $z \sim 1$ elongated galaxies do not show strong rotation, implying that ellipticity is not always a good measure of inclination, or that some galaxies are not rotating disks, or both. Because the conventional assumptions about inclined rotating disks may break down, using galaxy ellipticity to perform inclination corrections on a sample of integrated linewidths σ_{1d} is not necessarily justified. However, any unrestricted sample of galaxies does include a range of inclinations, so the mean value of σ_{1d} is reduced by some factor when inclination corrections are not applied.

3. THE TULLY-FISHER RELATION FOR INTEGRATED LINEWIDTHS

3.1. Tully-Fisher relations in redshift subranges

We combine the absolute magnitudes and the line-of-sight linewidths of integrated emission σ_{1d} to produce the Tully-Fisher relations for integrated linewidths shown in Figure 1 for B -band and Figure 2 for J -band. The sample is broken into several redshift ranges. In each figure, the large points show weighted and unweighted means of $\log \sigma_{1d}$ in bins of magnitude. The diagonal lines are maximum likelihood fits, described below, to the observed linewidths σ_{obs} in each redshift range; we fit to σ_{obs} to mitigate numerical issues caused by the subtraction of instrumental resolution, discussed below. The low redshift fit (dashed line) is plotted in all four redshift ranges for comparison. The fits are restricted to

galaxies brighter than $M_B = -18$ and $M_J = -19$ respectively. Below these magnitude limits, σ_{1d} becomes small, comparable to random non-gravitational motions, and difficult to measure, and the linearity of the observed Tully-Fisher relation in σ_{1d} is dubious.

There is clear evolution in the B -band Tully-Fisher relation: at high redshift, galaxies lie to the right of or below the low- z line (brighter or lower velocity). We discuss fitting methods and interpretations of the evolution below.

In these and all subsequent figures and discussion of the Tully-Fisher relation, we plot, fit and discuss velocity as a function of magnitude, $V(M)$. For these high-redshift galaxies, the primary selection boundary is the magnitude limit, and the errors are larger on velocity than on magnitude. For local galaxies, the convention is often to treat luminosity as a dependent variable, in part due to the history of the TF relation as a distance indicator. Taking velocity as the dependent variable is often called the “inverse Tully-Fisher relation” (Fouque et al. 1990). We always perform fits that take both errors into account, so there is not an independent/dependent distinction in the fit, but the magnitude selection introduces an asymmetry that makes fitting $V(M)$ more sensible. The reader should keep in mind that the slope of the fit lines in Figures 1 and 2 is opposite the sense in which $M(V)$ Tully-Fisher relations are usually described as shallow or steep.

Figure 1 plots the galaxies in the “good linewidth” sample individually as small points. The large points in Figure 1 show the weighted and unweighted means of $\log \sigma_{1d}$ in magnitude bins; the error bars indicate the RMS within each bin (not the error of the mean). Large points are only plotted for bins with ≥ 5 galaxies. The mean-in-bins points show that there is a clear relation of velocity with magnitude within each redshift range, and that in B , this relation evolves with redshift.

There is a significant scatter induced by intrinsic scatter in the TF relation, and secondarily by errors on the individual velocity measurements. For galaxies with $M_B < -18$, the intrinsic scatter about the fitted relations is 0.18 dex in $\log \sigma_{1d}$, and the median observational error is 0.084 dex. Intrinsic scatter in the $\log \sigma_{1d}$ TF relation could come from scatter in true properties of the galaxies, from the transformation from detailed galaxy kinematics to integrated linewidth, and from the lack of inclination correction. In Section 4.3 of Paper I we showed that for idealized circular rotating disks, omitting inclination and extinction corrections leads to scatter of ~ 0.19 dex in a B -band TF.

However, the similarity between the idealized and measured scatter is fortuitous. When we use the ellipticities from HST/ACS imaging to infer inclination and extinction corrections for the $M_B < -18$ sample, we find that the intrinsic scatter about fitted TF relations *does not decrease*.⁹ The scatter increases minutely from 0.18 to 0.19 dex. The likely cause is that there are a significant number of galaxies that are not consistent with circular rotating disks, as discussed in Paper I. For these galaxies, inclination corrections to velocity may be inappropriate

⁹ For the fits comparing the effect of inclination and extinction corrections, we exclude galaxies with ellipticity $e < 0.2$, to avoid large corrections to velocity width.

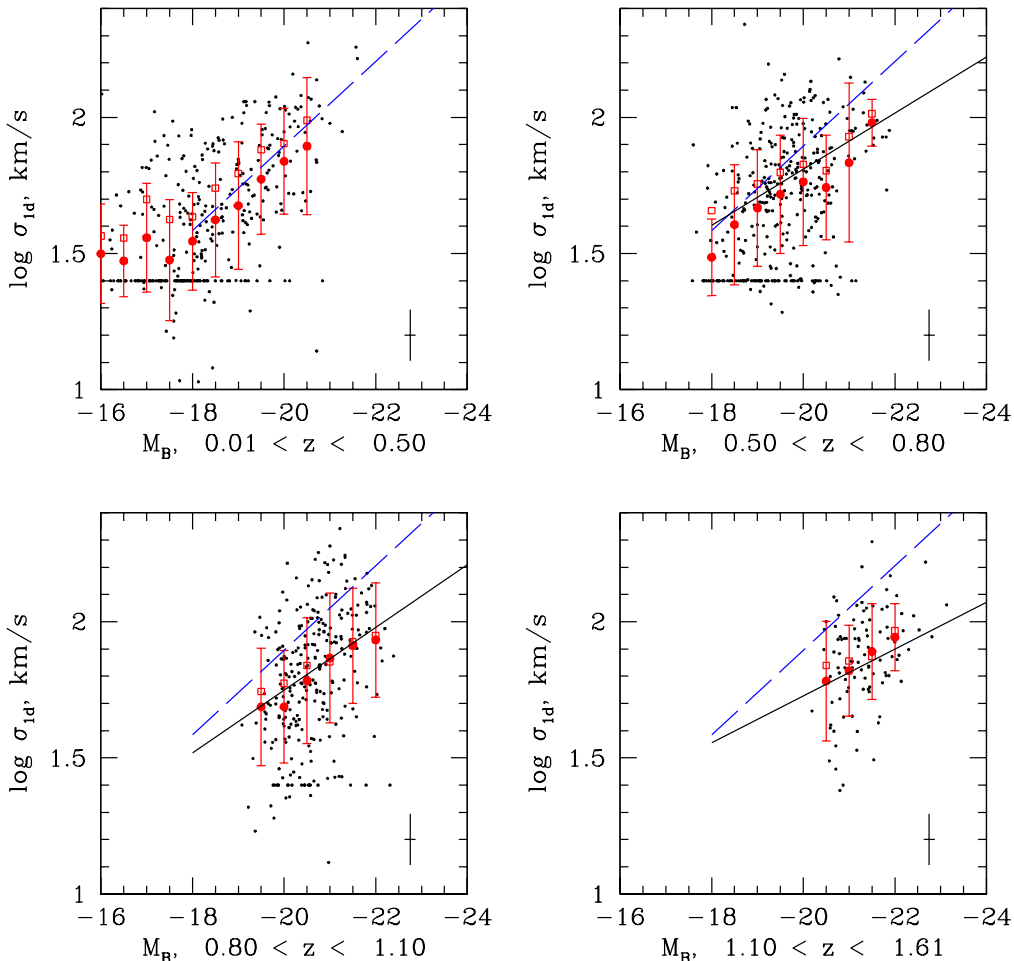


FIG. 1.— The Tully-Fisher relation in the TKRS for integrated line-of-sight linewidth and rest B magnitude, in four redshift ranges. Individual galaxies are plotted as small points. Large circles and errorbars are the unweighted mean and RMS in magnitude bins; large squares are the weighted mean. The small points at $\log \sigma_{1d} = 1.4$ are kinematically unresolved galaxies. The dashed diagonal line is a fit to the low-redshift range for $M_B < -18$, and is repeated in all four panels. The solid diagonal lines are fits to the higher redshift ranges. The cross in the lower right corner of the plots shows the median observational errors. At high redshifts, nearly all the galaxies fall below or to the right of the low-redshift relation.

and/or ellipticities may not give proper inclinations. We discuss TF scatter further in Section 4. Because it is not clear that the “corrections” are an improvement for this sample, which is not restricted to disk morphologies, we refrain from applying them.

3.2. Fitting the Tully-Fisher relation: methods and sample

In each redshift range, we fit linear Tully-Fisher relations with the ridgeline

$$\log \sigma_{1d} = A_\lambda + B_\lambda(M_\lambda - M_{zp,\lambda}), \quad (2)$$

with intrinsic scatter C_λ in $\log \sigma_{1d}$. The TF relations are zeropointed at $M_{zp,B} = -21$ and $M_{zp,J} = -22$ to decrease covariance between intercept A and slope B . We used a maximum likelihood method (hereafter MLS, for maximum likelihood with scatter) to fit the Tully-Fisher relation to data that have intrinsic scatter and errors in

both coordinates. The MLS method is derived in the Appendix, and tests of fitting methods are discussed in Section 3.5.

The MLS method treats the TF relation with scatter as a model probability distribution, and convolves the model with the error distributions of the observations to compute a conditional probability of the model given the data. For a linear ridgeline and gaussian scatter and errors, the MLS method becomes mathematically very similar to a generalized least squares (GLS) method, based on the `fitexy` routine (Press et al. 1992). GLS performs a least-squares fit by adding the intrinsic scatter to the error in the y -coordinate, here taken to be the velocity (see Tremaine et al. 2002; Novak, Faber & Dekel 2005; Pizagno et al. 2005; Bamford et al. 2006). The MLS method places this *ad hoc* extension on a firmer statistical footing, and yields nearly identical fit results.

Because some of the galaxies are kinematically un-

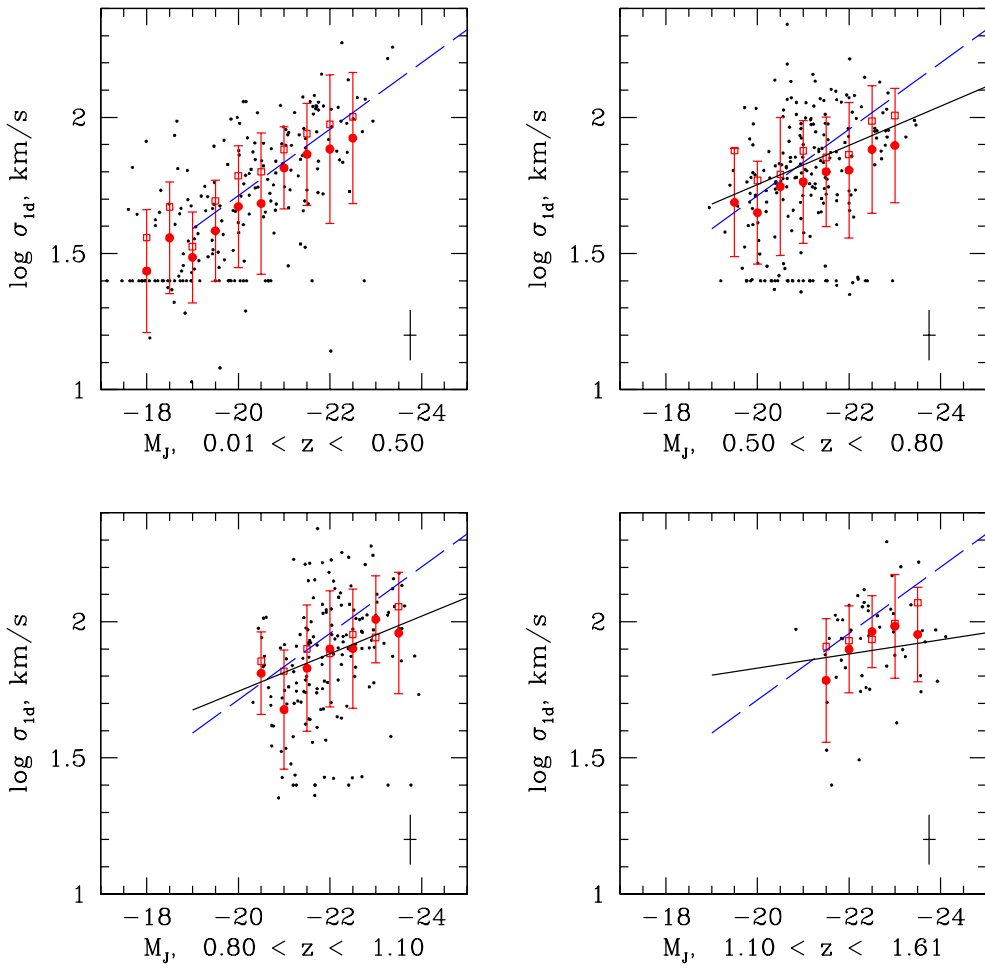


FIG. 2.— The Tully-Fisher relation in the TKRS for integrated line-of-sight linewidth and rest J magnitude, in four redshift ranges. Individual galaxies are plotted as small points. Large circles and errorbars are the unweighted mean and RMS in magnitude bins; large squares are the weighted mean. The small points at $\log \sigma_{1d} = 1.4$ are kinematically unresolved galaxies. The dashed diagonal line is a fit to the low-redshift range for $M_J < -19$, and is repeated in all four panels. The solid diagonal lines are fits to the higher redshift ranges. The cross in the lower right corner of the plots shows the median observational errors. The J -band relation shows less evolution than in the B -band.

resolved, we perform the MLS fits by convolving the model distribution with the data in the space of observed linewidth σ_{obs} rather than intrinsic dispersion σ_{1d} . This enlarges the samples with good measurements slightly, to 968 galaxies brighter than $M_B = -18$, and 677 brighter than $M_J = -19$, each with a σ_{obs} measurement from its strongest emission line. The best-fit relations in each redshift range from these fits are shown in Figures 1 and 2. The best-fit intercept and slope are listed in Table 1 and plotted against redshift in Figures 3 and 4. The best-fit values from fitting directly in σ_{1d} space are statistically similar, as long as the kinematically unresolved objects are included by setting them to the arbitrary value of $\log \sigma_{1d} = 1.4$.

The MLS method can fit A , B , and C together; here we fixed the intrinsic scatter at $C = 0.18$ dex, which is the best value for the entire sample in both B and J . The TF slope and intercept are only very weakly dependent

on the scatter, as long as the assumed scatter is reasonable (within a factor of 1.5–2). Because the scatter is sensitive to the error estimates, and there are a significant number of kinematically unresolved galaxies, and the sample is not extremely large, we do not trust it to measure evolution in the scatter.

3.2.1. Properties of the data set

There has been some argument over proper methods for fitting Tully-Fisher and similar relations (see Willick 1994), and a related controversy has flared briefly in the field of black hole masses (see Tremaine et al. 2002; Novak et al. 2005). It is not our intention to present a solution for fitting model relations to data that works in all cases, but to present a well-posed model that can be constrained fairly and applied to our dataset. We list here some salient features of high-redshift Tully-Fisher relations and our dataset in particular. Section 3.5 tests the reliability of fitting methods using simulated data

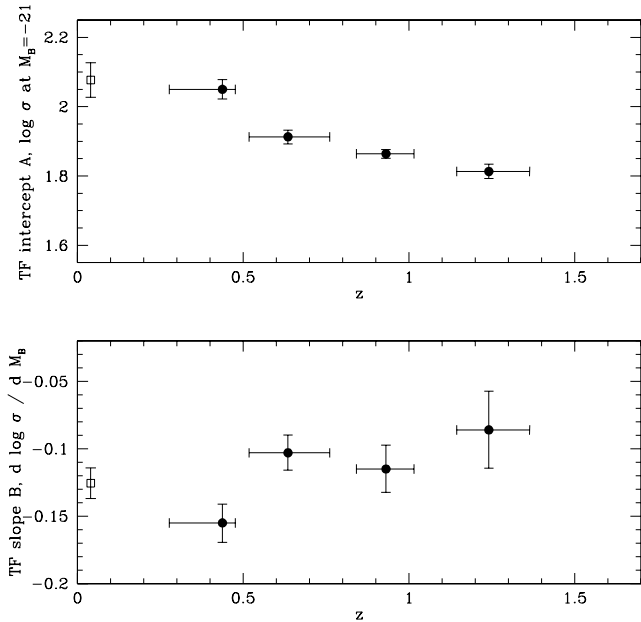


FIG. 3.— Redshift evolution of the B -band Tully-Fisher intercept and slope, $\log \sigma_{1d} = A_B + B_B(M_B + 21)$. The intercept and slope are fitted with the MLS maximum likelihood method as described in Section 3.2 in four redshift ranges. The points are plotted at the median redshift of the range and the horizontal bars are the 68% range in redshift. The local B -band TF intercept and slope of Sakai et al. (2000) are plotted at low z for comparison.

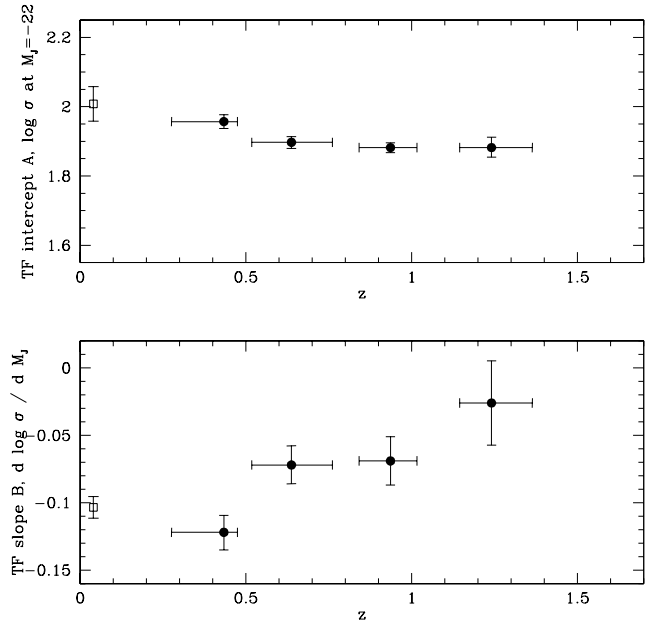


FIG. 4.— Redshift evolution of the J -band Tully-Fisher intercept and slope, $\log \sigma_{1d} = A_J + B_J(M_J + 22)$. The intercept and slope are fitted with the MLS maximum likelihood method as described in Section 3.2 in four redshift ranges. The points are plotted at the median redshift of the range and the horizontal bars are the 68% range in redshift. The local J -band TF intercept and slope of Watanabe et al. (2001) are plotted at low z for comparison.

that reproduces these properties.

1) The data available in high- z TF relations are strongly selected in magnitude. A sample is unlikely to cover more than ~ 3 magnitudes at any given redshift: the faint limit is set by S/N and the bright limit is set by the lack of galaxies brighter than M^* , and the magnitude range of a sample narrows at higher redshift. However, there is not a strong selection on velocity. The selection limits make it more straightforward to use the “inverse” TF relation in which magnitude is the independent variable.

2) The (inverse) Tully-Fisher relation has a shallow slope. Typical slopes of log velocity on magnitude are 0.125 to 0.09 from B to K ; $\log V = (0.31 \text{ to } 0.23) \log L + \text{const}$ (e.g. Tully et al. 1998; Sakai et al. 2000).

3) At high z , observational errors on log velocity or dispersion are larger than errors on magnitude, when the slope is taken into account. Our median errors are 0.084 dex in $\log \sigma_{1d}$, 0.12 mag in M_B , and 0.14 mag in M_J , but since the slope is 0.08 – 0.15 dex/mag, the errors on $\log \sigma_{1d}$ are effectively 4 – 9 times larger than on magnitude. Fortunately, the large velocity errors scatter along the magnitude selection limit rather than across it.

4) The intrinsic scatter in the high- z Tully-Fisher relation is large. This is especially true for a sample like ours which is not highly selected on morphology, kinematic regularity, or other properties, and also not corrected for inclination. Fitting methods which do not take into account intrinsic scatter are generally biased, especially in slope.

5) The TKRS resolution of 1.4 \AA is only moderately

high, so some low-linewidth objects are kinematically unresolved, and others which are barely resolved have large fractional error on σ_{1d} . Therefore the error on σ_{1d} , and even more so on $\log \sigma_{1d}$, is inversely correlated with σ_{1d} . This can lead to biases in fitted relations and weighted means: the weighted mean of $\log \sigma_{1d}$ will be biased high if gaussian errors on $\log \sigma_{1d}$ are assumed. Fitting in wavelength space σ_{obs} partially mitigates this bias.

A correlation between $\log \sigma_{1d}$ and error on $\log \sigma_{1d}$ shows up as an offset between weighted and unweighted means of $\log \sigma_{1d}$. The binned points in Figures 1 and 2 show that this offset exists in the $0 < z < 0.5$ data but is relatively small in the higher redshift data. Because we use a fit method that accounts for both the errors on individual points and the intrinsic scatter, the best fit line lies between the weighted and unweighted means.

6) The raw observational errors on velocity and magnitude are independent. However, transforming to deprojected properties can make the errors covariant; inclination and extinction corrections are highly correlated.

3.2.2. Magnitude-limited samples

We only include galaxies brighter than $M_B < -18$ or $M_J < -19$ in the Tully-Fisher fits, for two reasons. First, very low luminosity galaxies are not visible at higher redshift and we want to keep the samples comparable. Second, the low luminosity galaxies have very low dispersion, close to the random velocities in H II regions and at the limit of what we can resolve, so there is effectively a minimum linewidth. Faint galaxies tend to scatter up in dispersion and would flatten the TF relation slope if

included in the fits; this effect is seen in the low-redshift panel of Figure 1.

Because we are fitting TF relations over a wide redshift range, the relative depth of the sample varies as a function of z . Since the sample is selected in observed R band, the changes in K -correction with redshift also change the slope of the magnitude limit with restframe color, as shown in Figure 3 in Paper I. Redder galaxies are progressively more disfavored at higher redshift. To match samples of similar galaxies at different redshifts, we constructed a near volume-limited sample. This sample meets a rolling magnitude cut that corresponds to the limiting color-magnitude line at $z = 0.9$, and tracks the luminosity evolution of the blue galaxy population by evolving by 1.3 magnitudes per unit redshift, as does L^* (Willmer et al. 2006). The magnitude limit has a constant slope with color, to guard against spurious trends that might be induced by favoring bluer galaxies at high redshift. The restricted sample is approximately volume limited with respect to mass for $z < 0.9$, if we assume that the primary evolution is fading in luminosity. This assumption is not proven, but the blue LF evolution and our discussion of models in Section 6.2 provide some evidence for it.

The equation of the cut is $M_B < -18.5 - 2 * (U - B) + 1.3 * (0.9 - z)$, and it is shown as the diagonal lines in Figure 3 of Paper I. We also restricted the sample to galaxies on the blue side of the color bimodality, with $U - B < 0.95$. 659 galaxies meet these cuts and have acceptable $\log \sigma_{1d}$ meeting the error cuts described previously; of these 49 are kinematically unresolved. For the fits done in wavelength space σ_{obs} , 672 galaxies meet the cuts. The best fit B -band TF parameters for the $M_B < -18$ and the rolling magnitude limit samples are listed in Table 1. The differences between the samples are minor at most; only the difference in the intercept A in the lowest redshift range is marginally statistically significant.

When we split the sample into aligned and misaligned samples based on slit alignment with the galaxy major axis, the fits are not significantly different within the errors, consistent with the lack of dependence of $\log \sigma_{1d}$ on slit alignment shown in Section 4.4 of Paper I.

3.3. Results: redshift evolution in the Tully-Fisher relation

Figures 1 and 2 show the redshift evolution of the Tully-Fisher relation for integrated linewidths. It is clear that in B -band, either galaxy properties or the relation of observables to properties are evolving, since almost all the points in the last redshift range lie below or to the right of the low-redshift relation. Here the size of our sample is important, since we can measure evolution within the sample and do not have to rely solely on calibrating the intercept to a local relation.

At higher redshifts, the galaxies fall below or to the right of the low-redshift fit line in B , meaning they have lower velocities or are brighter. In J -band, the offset between high-redshift points and low-redshift fit is smaller than in B . The remainder of this paper is devoted to quantifying the evolution in intercepts and slope, determining whether it is a change in the basic physical properties of galaxies or only a change in the kinematic tracers, and presenting a few toy models for evolution in

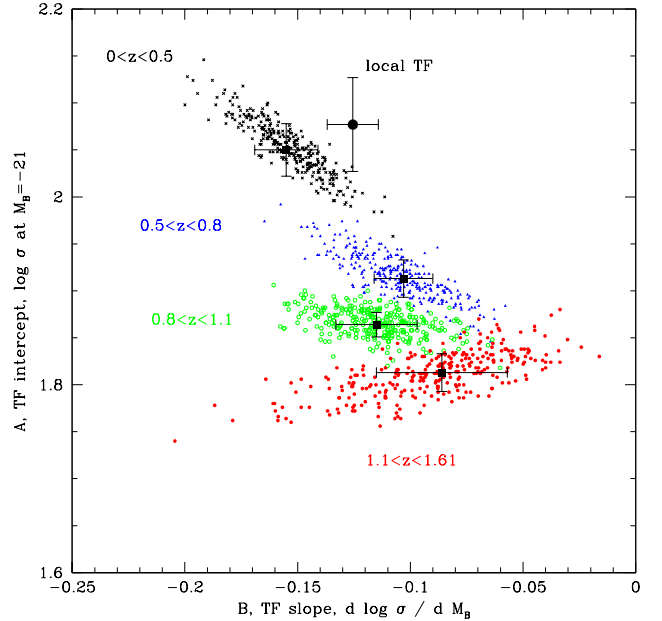


FIG. 5.— Error estimation on B -band Tully-Fisher parameters slope B versus intercept A in four redshift ranges. Each point represents a fit to one of 300 bootstrap resamplings of the data in that z range, and the locus of points indicates the covariance and scatter in the parameters; Xes are $0 < z < 0.5$, triangles $0.5 < z < 0.8$, open circles $0.8 < z < 1.1$, and filled circles $1.1 < z < 1.61$. The filled squares and error bars near the centers of the bootstrap distributions show the best-fit values from Table 1. The local B -band intercept (converted to σ_{1d}) and slope are shown as the large point (Sakai et al. 2000). Intercept and slope are quite covariant in the $0 < z < 0.5$ sample. There is clear evolution in intercept with redshift, and some evidence for evolution in slope.

the TF relation.

The upper panels of Figures 3 and 4 show the evolution in TF intercept A as a function of redshift in B and J -bands, and the intercept of local TF relations for comparison (Sakai et al. 2000; Watanabe et al. 2001). Here and afterwards we show results from the full samples with $M_B < -18$ and $M_J < -19$.

There is substantial evolution in the B -band intercept, internal to our sample and compared to the local sample. However, there is relatively little evolution in the J -band intercept. These agree with the visual impression of Figure 1, where most of the high-redshift galaxies lie below or to the right (brighter M_B) of the low-redshift fit, while in Figure 2 the high-redshift galaxies are not very offset from the low-redshift fit.

For the local TF relations, we transform the relations from inclination-corrected H I width $W_{20,corr}$ to the intercept A in $\log \sigma_{1d}$. We assume $\sigma_{1d} = 0.28W_{20}$ (Kobulnicky & Gebhardt 2000), and decorrect the local TF relations by the median inclination and extinction corrections for a randomly oriented sample, using extinctions $A_{B,ext} = 1.57 \log(a/b)$ and $A_{J,ext} = 0.736 \log(a/b)$, as used in the local TF relations, but omitting velocity-dependence of extinction.¹⁰ The median inclination for

¹⁰ Extinction corrections that depend on velocity tend to change the B -band slope by about 10% and the J -band slope relatively

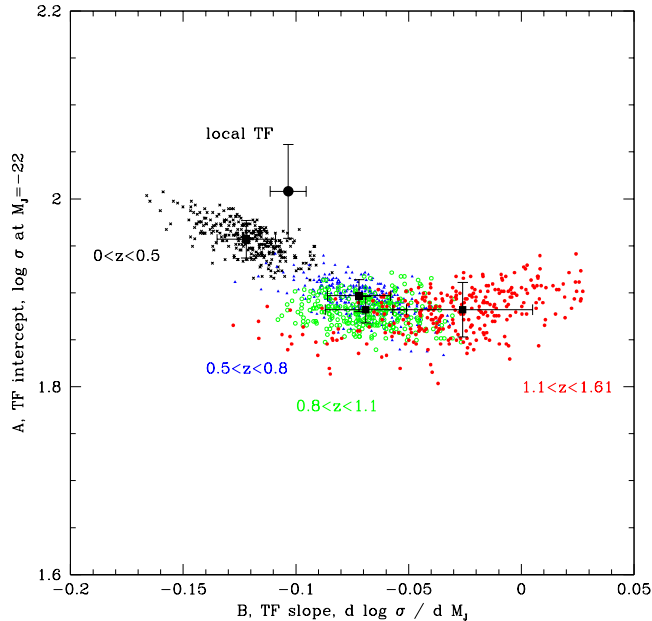


FIG. 6.— Error estimation on J -band Tully-Fisher parameters slope B versus intercept A in four redshift ranges. Each point represents a fit to one of 300 bootstrap resamplings of the data in that z range, and the locus of points indicates the covariance and scatter in the parameters; Xes are $0 < z < 0.5$, triangles $0.5 < z < 0.8$, open circles $0.8 < z < 1.1$, and filled circles $1.1 < z < 1.6$. The filled squares and error bars near the centers of the bootstrap distributions show the best-fit values from Table 1. The local J -band intercept (converted to σ_{1d}) and slope are shown as the large point (Watanabe et al. 2001). Evolution in intercept is weak, but there is evidence for evolution in slope.

a randomly oriented sample is 60° , so that the median $\langle \log \sin i \rangle = -0.0625$ and $\langle \log(a/b) \rangle = 0.30$. We assigned a systematic error of 0.05 dex to this conversion from $W_{20,corr}$ to A ; error in the conversion dominates over the statistical errors in the local fits. Other local B -band TF relations lie in essentially the same place as the Sakai et al. relation (e.g. Tully & Pierce 2000).

The lower panels of Figures 3 and 4 plot the trend of slope B_λ with redshift, and show some evidence for TF slope evolution, seen in the fits plotted in Figures 1 and 2. The $z > 0.5$ redshift points all have shallower inverse-TF slopes than both the low redshift points and the local B and J -band TF relations. In the B -band, the total significance of the high- z slope offsets from our $0 < z < 0.5$ value is 3.0 sigma.¹¹ The J -band shows a similar trend, though there are too few galaxies in the J -band sample at $z > 1.1$ to measure a reliable slope.

Figures 1 and 3, and Table 1 show that there is evolution in both the intercept and slope of the B -band linewidth Tully-Fisher relation. In the lowest redshift range, the slope is $B = -0.155 \pm 0.014$, or $-1/B = 6.5 \pm 0.6$, at most modestly different from local measurements of the B -band Tully-Fisher slope, e.g. $-1/B = 7.3$

little. We avoid using any velocity-dependent extinction for the linewidth TF relation because our velocity measure is noisy and it could induce spurious correlations.

¹¹ A similar slope evolution is found in the forthcoming larger DEEP2 sample, which will provide a more precise measurement.

(Tully & Pierce 2000) or 8.0 ± 0.7 (Sakai et al. 2000). Given the effects on slope of inclination-induced scatter (Section 4.3 of Paper I), velocity-dependent extinction, and the covariance between A and B shown in Figure 5, the intercept and slope in our lowest redshift range are not significantly different from the local values.

The B -band TF evolution appears to be strongest from low redshift to $z \sim 1$, but covariance of slope and intercept plays a role here, as shown in Figure 5. It is possible that our $0 < z < 0.5$ range has an intercept A that is a bit too high and a slope B that is a bit too steep, compared to the local values. This could arise in part from the correlation of $\text{error}(\sigma_{1d})$ and σ_{1d} , point 5 of Section 3.2.1.

Because the fit parameters A and B are covariant, we show confidence regions generated by bootstrap resampling in Figures 5 and 6, to give a more complete picture of the evolution of TF parameters. For each of the four redshift ranges, we generated 300 samples with replacement from the original data and refit these samples. The loci of points indicate the error ranges and covariance. Intercept evolution is very significant in B -band, but only significant in J if the local sample is used as the calibrator. The fits suggest, at $\sim 3\sigma$, that the high-redshift slope B_λ is shallower in velocity on magnitude $V(M)$ in both bands; they provide a strong rejection of the idea that the high-redshift slope is steeper in $V(M)$.

Galaxies at higher redshift have lower $\log \sigma_{1d}$ at a given magnitude, or equivalently a brighter magnitude at a fixed dispersion. The luminosity evolution is physically more likely than velocity evolution, assuming that we are seeing evolution in the global properties of galaxies rather than just in the properties of σ_{1d} as a kinematic tracer, as discussed further in Section 5. Stellar populations are well-known to evolve in luminosity, while the characteristic density and velocity of the inner part of a galactic halo change little at late stages of its mass accretion history, because late-time accreted mass is relatively low density (Wechsler et al. 2002). The fact that evolution is stronger in the B -band than in the J -band supports the interpretation of luminosity evolution.

Since there appears to be slope evolution, the amount of magnitude evolution is itself a function of magnitude. In the highest redshift range, with median $z = 1.2$, a galaxy with $M_B = -22$ must fade by ~ 2 mag to reach the low-redshift $z = 0.4$ TF relation, while a galaxy with $M_B = -20$ must fade by only 1.2 mag. These numbers will be reduced by ~ 0.5 mag if the $z = 0.4$ relation is biased high in intercept as discussed above. We discuss models for differential luminosity evolution in Section 6.2.

The intrinsic scatter of 0.18 dex in $\log \sigma_{1d}$ converts to ~ 1.5 magnitudes of intrinsic scatter. This scatter is significantly larger than in low-redshift Tully-Fisher relations; most of these are restricted in morphology, and have scatter from 0.25–0.55 mag (e.g. Tully et al. 1998; Willick 1999; Sakai et al. 2000), although Kanapanan, Fabricant & Franx (2002) find an intrinsic scatter of 0.5–0.6 mag in B for bright spirals only but 0.8–0.9 mag in a sample which includes dwarfs and is not pruned on morphology. There are several reasons for our high scatter, including: lack of inclination and extinction corrections; our use of linewidth instead of circular velocity; and an all-inclusive sample that is broader than

TABLE 1
BEST-FIT TULLY-FISHER RELATIONS

Band	Sample	Number	Redshift range	Median redshift	Zeropoint (mag)	Maximum likelihood fit ^a intercept A_λ slope B_λ	
<i>B</i>	$M_B < -18$	218	$0.07 < z < 0.5$	0.437	-21	2.050 ± 0.028	-0.155 ± 0.014
<i>B</i>	$M_B < -18$	374	$0.5 < z < 0.8$	0.635	-21	1.913 ± 0.020	-0.103 ± 0.013
<i>B</i>	$M_B < -18$	280	$0.8 < z < 1.1$	0.931	-21	1.864 ± 0.013	-0.115 ± 0.018
<i>B</i>	$M_B < -18$	96	$1.1 < z < 1.61$	1.241	-21	1.813 ± 0.020	-0.086 ± 0.029
<i>B</i>	Blue + magcut ^b	87	$0.11 < z < 0.5$	0.438	-21	2.007 ± 0.037	-0.154 ± 0.028
<i>B</i>	Blue + magcut	237	$0.5 < z < 0.8$	0.679	-21	1.923 ± 0.024	-0.119 ± 0.020
<i>B</i>	Blue + magcut	252	$0.8 < z < 1.1$	0.927	-21	1.864 ± 0.013	-0.122 ± 0.018
<i>B</i>	Blue + magcut	96	$1.1 < z < 1.61$	1.241	-21	1.813 ± 0.020	-0.086 ± 0.029
<i>J</i>	$M_J < -19$	165	$0.09 < z < 0.5$	0.433	-22	1.957 ± 0.020	-0.122 ± 0.013
<i>J</i>	$M_J < -19$	232	$0.5 < z < 0.8$	0.637	-22	1.897 ± 0.017	-0.072 ± 0.014
<i>J</i>	$M_J < -19$	165	$0.8 < z < 1.1$	0.936	-22	1.882 ± 0.014	-0.069 ± 0.018
<i>J</i>	$M_J < -19$	50	$1.1 < z < 1.53$	1.241	-22	1.882 ± 0.029	-0.026 ± 0.031

^aMaximum likelihood fits with TF scatter of 0.18 in $\log \sigma_{1d}$.

^bBlue+magcut sample restricted to $U - B < 0.95$, and color-magnitude limit evolving as L^* with redshift: $M_B < -18.5 - 2(U - B) - 1.3(z - 0.9)$.

low-redshift samples, which are often highly selected to favor undisturbed, orderly inclined disks. However, high- z Tully-Fisher morphologically selected and inclination-corrected rotation curve samples also show larger scatter than at low- z , discussed further in Section 4.

3.4. Tully-Fisher relation for rotation curves

We can also construct Tully-Fisher relations using the spatially resolved measures of velocity and dispersion, V_{rot} and σ_{2d} , measured with the ROTCURVE program on a subset of the 2-d spectra as discussed in Paper I. Paper I demonstrated that there are rotation and dispersion dominated galaxies (RDGs and DDGs), in which V_{rot} or σ_{2d} is respectively more important. The dispersion σ_{2d} can represent disordered kinematics or other velocity variations on scales below the seeing limit. For the combined velocity measures $S_{1.0}$ and $S_{0.5}$, where $S_K^2 = KV_{rot}^2 + \sigma_{2d}^2$, fitting yields TF results that are similar to the 1-d dispersion TF relation and its evolution, albeit noisier since the sample is one-third as large. The similar TF results are expected since $S_{1.0}$ and $S_{0.5}$ correlate well with σ_{1d} . The RDGs and DDGs show similar residual trends with redshift; at $z \sim 1$ both are shifted brighter than their low-redshift counterparts. There is a small residual in the σ_{1d} Tully-Fisher relation as a function of V_{rot}/σ_{2d} or RDG/DDG-ness, discussed further in Section 5.1.2.

The Tully-Fisher relation measured in the line-of-sight rotation velocity V_{rot} is also of interest. Although V_{rot} does not capture the full kinematic support of DDGs, the V_{rot} TF relation is most analogous to rotation velocity measurements made in other works. Figure 7 shows the B -band TF relation for V_{rot} , restricted to galaxies with ellipticity $e > 0.25$ and aligned slits. There are not many galaxies in this sample, and we are only brave enough to fit a TF relation in the lowest redshift bin; the low- z fit is repeated in the other bins for comparison. The low- z fit has $A_{B,V_{rot}} = 2.060 \pm 0.145$ and $B_{B,V_{rot}} = -0.134 \pm 0.081$, with covariant errors. Its slope is consistent with local Tully-Fisher relations, and its intercept is marginally lower in velocity, after compensating for the lack of inclination and extinction correc-

tions. At least some of this offset is likely due to galaxies with low V_{rot} that are not dominated by orderly rotation and would be excluded from local TF samples. We have applied no inclination correction in Figure 7, but since $e > 0.25$, $\sin i > 0.66$, and the range of possible corrections is limited. The low-velocity objects in Figure 7 are something other than face-on disks.

As in the 1-d linewidth-magnitude TF relation, high-redshift points fall below or to the right of the low- z V_{rot} -magnitude relation. The range of velocities observed is similar at low and high redshift, suggesting that the evolution is more in the sense of brighter galaxies at high redshift, rather than a lack of high-velocity galaxies at high z . The similar behavior in the 1-d linewidth σ_{1d} relation provides evidence that its evolution is real rather than a changing property of the relation between 1-d linewidth and rotation velocity.

The scatter in this TF relation for rotation curves is quite large, ~ 0.3 dex. Inclination correction does not reduce it much because the sample was already restricted to $e > 0.25$, so the range of possible correction to velocity is 0 to 0.18 dex. The scatter is high not because individual measurements are bad, but because the sample has not been pre-selected to include only morphologically ordinary, orderly rotating disks. A significant amount of the scatter is due to low-velocity objects. These are dispersion-dominated galaxies (see Paper I) with a component of kinematic support due to random or disordered motions below the seeing limit. Because they are not primarily supported by an observed rotation gradient, V_{rot} underestimates their kinematic support. However, simply eliminating DDGs from a TF sample is fraught with danger because it preferentially excludes low-velocity galaxies, introducing a selection on V_{rot} .

3.5. Testing fitting methods: fitting, scatter, and incompleteness biases

Methods for fitting linear relations such as Tully-Fisher have sometimes been controversial. Several biases can arise, caused by observational errors, intrinsic scatter, and magnitude limits. Biases can be exacerbated in the high-redshift TF relation by the large intrinsic scatter.

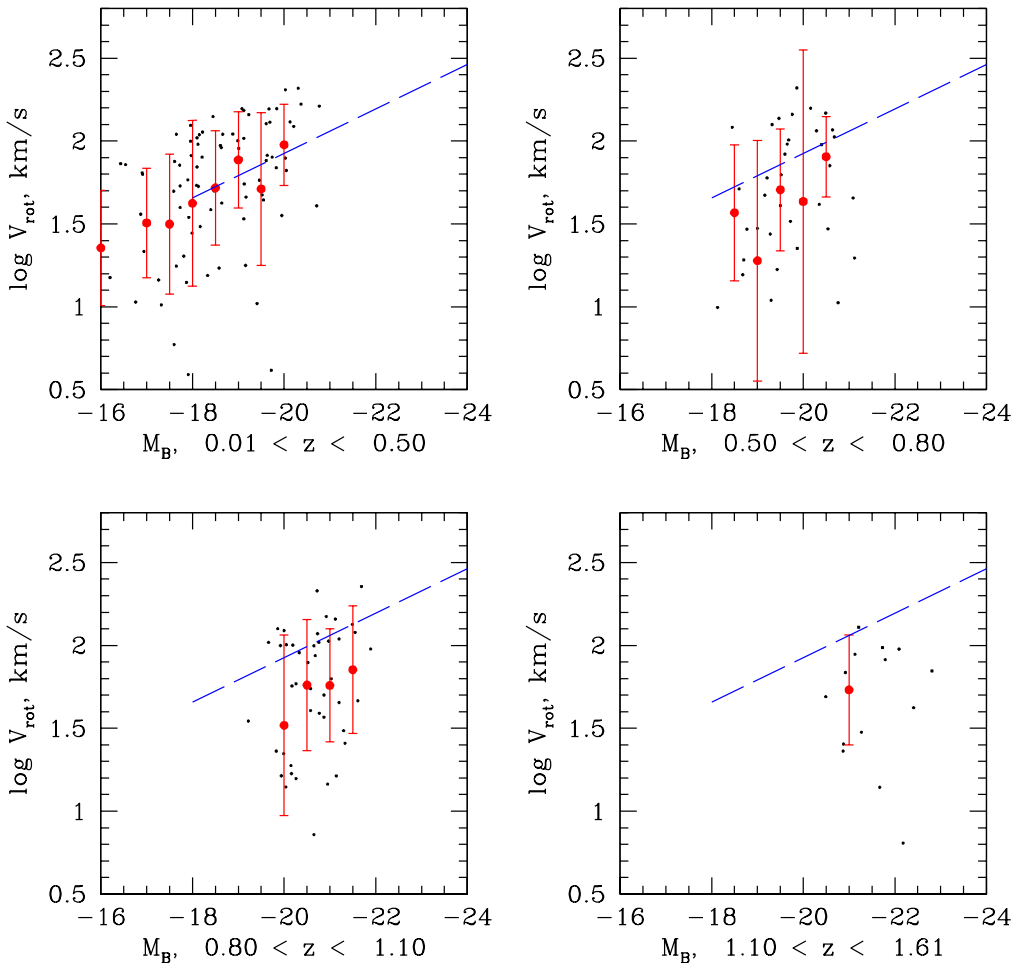


FIG. 7.— The Tully-Fisher relation in the TKRS for line-of-sight rotation velocity and rest B magnitude, in four redshift ranges, for the galaxies in the ROTCURVE sample with aligned slits and ellipticity $e > 0.25$. Corrections for inclination and extinction are not applied. Individual galaxies are plotted as small points. Large points and error bars are the mean and RMS in magnitude bins. The dashed diagonal line is the fit to the low-redshift range, repeated in all four panels. As in the linewidth-magnitude relation, at high redshift galaxies are observed brightward or lower velocity compared to the low-redshift fit.

Here we describe tests of several fitting methods, to insure that the parameters listed in Table 1 are reliable.

3.5.1. Scatter-induced bias in least-squares fitting algorithms

A common method of fitting a linear relation to data with errors in both coordinates is the `fitexy` least-squares routine, derived from a χ^2 minimization (Press et al. 1992). The `fitexy` method does not model relations with intrinsic scatter, so yields formally rejectable fits with $\chi^2/N \gg 1$, and can yield biased results when there is scatter. A method that does account for scatter was proposed by Akritas & Bershady (1996), but this method has been criticized by Tremaine et al. (2002) and Novak et al. (2005). These authors in turn generalized the `fitexy` method by adding the intrinsic scatter as an effective error term in one of the coordinates, so that the best fit has $\chi^2/N = 1$. In the Appendix we show that this intuitive treatment (generalized least squares,

or GLS method) is derivable from a maximum likelihood model, a special case of the maximum likelihood (MLS) method we have used. None of these models explicitly compensate for effects caused by selection limits.

To test biases introduced by scatter and selection limits, we generated simulated data sets with Monte Carlo realizations. We took the true values of M_B in a single redshift range, enforced a TF relation with slope $B_{model} = -0.1$, and perturbed the points by gaussian random variates of the observational errors $\text{err}(M_B)$, $\text{err}(\log \sigma_{1d})$, and an intrinsic scatter C in $\log \sigma_{1d}$ of 0.15 dex. Measuring and applying the intrinsic scatter in $\log \sigma_{1d}$ rather than in M_B is required because the sample is magnitude selected, and sensible because the slope is shallow.

As the scatter C is increased, bias in some of the methods increases to be quite significant. For the `fitexy` method without accounting for intrinsic scatter, the fitted slope was typically $B_{model,fit} \sim -0.15$. We be-

lieve that the algorithm increases the slope to compensate for the additional scatter-induced dynamic range of the sample in $\log \sigma_{1d}$. However, the generalized least-squares GLS routine with scatter C added in quadrature to $\text{err}(\log \sigma_{1d})$ had no measurable bias in slope. The maximum likelihood MLS method described in the Appendix is nearly identical and also tested free of bias. The BCES($Y|X$) and BCES Orthogonal methods of Akritas & Bershady (1996) had a small bias, typically returning slopes $B_{fit} \sim -0.095$.

A sometimes-popular class of methods, the bisector fits (see e.g. Isobe et al. 1990; used for Tully-Fisher in Ziegler et al. 2002; Böhm et al. 2004) tested out to be extremely bad for this TF dataset when applied without regard for magnitude selection. Bisector fits perform two standard least-squares fits using one set of errors at a time, fitting ($Y|X, \text{err}(X)$) and ($X|Y, \text{err}(Y)$) to obtain two fit lines, and take the lines' bisector as the best fit. Two problems with this approach are: the two fits can have radically different χ^2 , but bisecting weights them equally; selection limits can strongly bias one of the fits, especially if the intrinsic scatter is large.

In our dataset, because (1) there is large intrinsic scatter; (2) the errors on $Y = \log \sigma_{1d}$ are larger than on $X = M_B$; and (3) most of all because the sample is highly selected in magnitude, the fit of Y on X is fairly good, while the fit of X on Y is terrible in χ^2 and in accuracy to the underlying relation. A typical Y on X fit yielded $B_{yx} = -0.098$, nearly correct, while the X on Y fit gave slope $1/B_{xy} = -1.18$, where -10 is correct. The bisector of these has slope $B_{bi,yx} = -0.42$, where -0.1 was correct; the effect of the bisector was to mix a bad fit in with a decent fit. Essentially, in a magnitude selected sample, determining the mean magnitude at a given velocity is only meaningful if the scatter and the velocity errors are very small, which is not the case in high-redshift TF samples. When the scatter is large, at a given velocity selection truncates the magnitude distribution, inducing a bias similar to Malmquist bias.

Accounting for intrinsic scatter within the fit method has two major effects. It removes biases such as the bias in slope we found for the unmodified, no-scatter `fitexy` method. Adding scatter also reduces the weight given to individual measurements with small error bars. For example, a measurement with \log velocity error 0.06 dex that deviates from our mean relation by 0.18 dex is a 3-sigma outlier when intrinsic scatter is neglected, but only a 1-sigma deviation given the intrinsic scatter.

An interesting consequence is that when a relation has large intrinsic scatter, sampling variation has a stronger effect on the observations than measurement noise. Measuring a TF relation that has significant scatter with a small number of non-noisy measurements is not efficient and can be misleading. Improvements in constraining a high-scatter TF relation come from either a larger sample or decreasing the intrinsic scatter, if possible. In some sense this is the familiar problem of overcoming cosmic variance by counting very large samples, but here applied to a regression problem rather than density estimation.

3.5.2. Incompleteness bias due to magnitude selection

The simulations described above test biases in the fitting methods due to scatter and due to the restriction in magnitude, but they do not rule out a type of bias in-

duced by sampling in the presence of a magnitude limit and magnitude errors. The ‘‘incompleteness bias’’ in truncated samples has been discussed in the local Tully-Fisher relation (e.g. Teerikorpi 1987; Willick 1994; Giovanelli et al. 1997; Tully & Pierce 2000), but less so for high-redshift samples. This bias is potentially important when using the forward TF relation as a distance indicator, since fitting magnitude on velocity is strongly affected by the magnitude limit, but that is not the case here since we use the inverse TF relation.

If errors in magnitude are zero, the bias is eliminated by fitting velocity on magnitude (Schechter 1980; Willick 1994; Tully & Pierce 2000). Our magnitude errors are non-zero, nearly ignorable but not quite. The bias can also be induced by inclination corrections which make velocity and magnitude covariant, but we do not apply those. One way this bias could affect the measurements is that faint galaxies that are scattered into the sample by observational errors tend to have lower velocities than slightly brighter galaxies that scatter out of the sample. Another possible effect is if the fitting methods which take into account magnitude errors react badly to the truncation of the data.

In practice, the most straightforward way to calibrate incompleteness bias is through Monte Carlo simulation (e.g. Giovanelli et al. 1997). We constructed samples by extending the magnitude distribution below our magnitude limit, forcing a TF relation with slope $B = -0.1$, applying the intrinsic scatter and observational errors, truncating the sample at the magnitude limit, and refitting. In the methods that treat scatter as an effective Y -error, incompleteness bias was undetectable relative to the variation among Monte Carlo samples, much smaller than the error estimates on A and B . The bias is small because the magnitude errors of ~ 0.12 mag are small compared to the 2-3 magnitude range of the sample, and the slope of velocity on magnitude is shallow.

4. COMPARISON TO OTHER TULLY-FISHER MEASUREMENTS

Several works have previously measured Tully-Fisher evolution, through either linewidths or rotation curve modeling. The picture has been confusing since methods, samples, and the amount of TF evolution found are different. Linewidth studies, each of ~ 20 galaxies, have generally found about 1-2 mag offset from the local Tully-Fisher relation at $z \sim 0.5$ (Forbes et al. 1996; Rix et al. 1997; Mallen-Ornelas et al. 1999). These results are difficult to interpret because the samples often were selected for high emission and because they were calibrated by reducing a local TF relation to linewidths, rather than internally. Pisano et al. (2001) suggested that these high-emission galaxies are vulnerable to linewidths that underestimate V_c ; we have tested for this effect with our spatially resolved fits in Paper I, and find little evidence for it in a sample that spans the whole of the blue population.

Rotation curve studies of DEEP 1 galaxies (Vogt et al. 1996, 1997; Vogt 2000; Conselice et al. 2005) found fairly little evolution, < 0.5 mag in B and < 0.3 mag in K , to $z \sim 0.7$. Flores et al. (2006) found little evolution in K in a sample highly selected on rotation properties. In contrast, Simard & Pritchett (1998) found ~ 1.5 mag evolution in B , in a sample selected to have moderately

high emission EW, with median $z \sim 0.4$. Bamford et al. (2005, 2006) found an evolution of 1.0 ± 0.5 mag in B projected to $z = 1$ in a sample of 89 galaxies with median $z = 0.4$.

Studies in the FORS Deep Field (FDF) claim to find relatively little evolution at high mass and 1-2 mag at low mass (Ziegler et al. 2002; Böhm et al. 2004). This is opposite the sense of differential evolution that we find; their high- z slope is steeper in $V(M)$, which is strongly rejected by our data. However, Kannappan & Barton (2004) argue that the evolution seen by the FDF group at the faint end is caused by kinematically anomalous galaxies. Bamford et al. (2006) show that the magnitude residuals are skewed in the FDF magnitude-limited sample, meaning that only the brighter low-mass galaxies are seen at high redshift. For this reason, the bisector method used in the FDF group’s TF fits yields biased slopes for samples with large scatter, as argued in Section 3.5. We performed MLS fits to the 77-galaxy sample of Böhm et al. (2004) and find inverse-TF slopes of 0.17 and 0.19 ± 0.03 dex/mag for the $z < 0.5$ and $z > 0.5$ galaxies respectively, with 0.4 ± 0.3 mag evolution in intercept (from median redshift 0.7 to 0.3), and 0.12 dex intrinsic scatter in $\log V_c$, in general agreement with the fit of Bamford et al. (2006) to the full Böhm et al. (2004) sample. These slopes are closer to the local value than the bisector fits were, and there is no evidence for slope evolution within the sample.

The amount of evolution that we find, $\sim 1.0 - 1.5$ mag evolution in B -band from $z = 0.4$ to 1.2, is larger than many of the rotation-curve samples. In part this may be because we have a larger number of galaxies at high redshift; although most of the rotation curve samples extend to $z = 1$, their median redshifts are ~ 0.5 . Another more significant issue is that the linewidth sample has fewer selection effects and can incorporate morphologically and kinematically unusual objects, especially the dispersion-dominated galaxies. Our sample is, in the mean, brighter than that of Vogt et al. (2000), and it is the brightest galaxies that show the most magnitude evolution. We speculate that the amount of luminosity evolution and degree of kinematic peculiarity could be linked.

Our linewidth TF relation has an intrinsic scatter of 0.18 dex or about 1.5 mag in B -band, which is large but about equal to the scatter predicted just from random inclinations of pure circular rotating disks (Section 4.3 of Paper I). However, as discussed in Section 3.1, the agreement with this inclination-induced scatter is fortuitous. Applying inclination and extinction corrections does not reduce the scatter. As suggested in Paper I, there could be many galaxies in the sample for which the kinematics are non-disk or the ellipticities yield misleading inclinations.

In fact, the contribution of dispersion or disordered motions to integrated linewidth probably reduces the inclination-induced scatter, because galaxies that are not ideal disks and have disorderly motions are less likely to fall to very low velocity when viewed face-on. However, the disordered motions may increase scatter induced by kinematic peculiarities, because the relation of the observed velocity to the halo mass is less direct. For inclination-corrected rotation curve samples, the Kannappan et al. (2002) local TF, which encompasses a wide range of galaxy types, has intrinsic scatter of 0.8–0.9

mag. Our fits to the Böhm et al. (2004) sample have an intrinsic scatter of 0.12 dex or ~ 0.7 mag. The rotation curve sample of Vogt et al. (2000) and Conselice et al. (2005) has a scatter of 0.7–1.1 mag even in K band, which usually has lower scatter than B . The subsample of Flores et al. (2006) that is restricted to orderly rotating galaxies has remarkably low scatter; these authors advocate the restriction of high-redshift TF samples to only orderly galaxies, but this would devalue the TF relation as an indicator of the evolution of the full blue galaxy population. Their larger sample including kinematically anomalous galaxies has a much larger scatter in V_{rot} , possibly in part because V_{rot} does not include the kinematic support from dispersion or disordered motions, as argued in Paper I.

In general, it appears that high-redshift TF samples have larger intrinsic scatter than the local TF relation, even when rotation curves are used. When linewidths are used and are not inclination corrected, the intrinsic scatter appears to increase, but not as much as one might expect from an ideal rotating disk model, because not all galaxies fit that model.

5. DISCUSSION: TULLY-FISHER EVOLUTION AND ITS CAUSES

The results of Section 3 show that there are Tully-Fisher relations between line-of-sight integrated linewidth $\log \sigma_{1d}$ and magnitudes M_B and M_J and that these relations evolve with redshift. The relations remain linear, with large scatter, within our ability to measure them. The data show a very strong detection of evolution in TF intercept in B -band, little evolution in intercept in J , and a moderately significant (3 sigma) evolution in the slopes. These measurements of evolution are internal to our sample; our $z \sim 0.4$ relations are fairly consistent, within the errors, with local TF relations after W_{20} is converted to σ_{1d} .

5.1. Selection effects versus real changes in galaxy properties

Several factors could cause evolution in the observed relations. The evolution could be induced by selection effects on the sample beyond simple magnitude selection, which we discussed in the previous section. The evolution could occur in the properties of integrated kinematics, e.g. in the σ_{1d}/V_{rot} ratio due to changes in galaxy velocity fields or emission distributions. Or the relation could reflect true evolution in the properties of galaxies, either in luminosity; or in measured velocity, which is determined by dynamical mass, radius, and concentration; or both.

5.1.1. Sample selection effects on TF evolution

In Section 3 of Paper I we showed that the sample of galaxies with linewidths is drawn evenly from the blue galaxy population in the TKRS. The fraction of blue galaxies without linewidths is small, $< 20\%$; since the missing galaxies are not systematically biased, they are too few to induce a significant bias in the measured relations. The differential evolution in the B -band TF relation means that the evolution is strongest for the brightest, easiest to detect galaxies; typical selection effects operate the opposite way.

The TF fits to the sample described in Section 3.2.2, with a rolling magnitude limit matched to the color-dependent magnitude limit at $z = 0.9$, are matched so that we are fitting to the same luminosity and color range of galaxies, relative to L^* , over a wide range of redshift. These TF fits, tabulated in Table 1, are very similar to the $M_B < -18$ sample. Thus the TF evolution measurement is not very sensitive to the location of the limit in the color-magnitude plane.

Because we are measuring the TF relation in galaxies with emission, effectively only in blue galaxies, one could imagine a selection effect caused by galaxies moving from the blue to red population as time increases. This would be a selection bias caused by a genuine evolutionary effect. The effect required to produce slope evolution is that among the brightest blue galaxies, preferentially the low-velocity ones would have to move to the red sequence. Then the (inverse) TF relation would steepen with time. This effect seems very unlikely. If anything, one would expect the opposite: the more massive, high-velocity galaxies should be older and stop star formation earlier.

It is very probable that mass is built up on the red sequence in part by galaxies which age, redden, and move from blue to red between $z \sim 1$ and now (Bell et al. 2004; Faber et al. 2006) and there are signs that the brightest blue $z \sim 1$ galaxies are on average located in dense environments, suggesting they will become red by the present day (Cooper et al. 2006). However, the blue galaxy luminosity function is consistent with an evolution in luminosity and relatively little evolution in number density in the same period (Willmer et al. 2006). If the percentage by number of blue galaxies which leave the sample is small, the effect of their departure on TF fitting is also small. TF relations with yet larger numbers of galaxies are needed to constrain the behavior of rare subpopulations.

5.1.2. Evolution in galaxy properties and residual correlations

The measured Tully-Fisher evolution could be an evolution in fundamental physical properties such as mass and luminosity, or an evolution in the relation of observables to properties, e.g. dispersion to rotation velocity, or rotation velocity to mass. It has been suggested that increased star formation in the centers of galaxies or compact galaxies at high redshift could cause integrated linewidths to underestimate rotation velocity (Pisano et al. 2001; Barton et al. 2001). Measurements of a variety of local galaxies (e.g. Kobulnicky & Gebhardt 2000) and the simulations presented in Section 4.2 of Paper I suggest that linewidth is actually a fairly robust measure, and that underestimating V_{rot} is only likely to be a problem in very extreme star-forming objects.

Our sample provides an empirical test. Figure 1 shows that the evolution we measure in B -band is if anything largest for the brightest galaxies. The brightest galaxies are also comparatively red even at high redshift, as the color-magnitude relation in Figure 3 of Paper I shows, while extreme star-forming objects are quite blue. It is hard to explain the measured TF evolution with an effect caused by extreme star formation episodes.

Another test comes from the color-TF residual relation in the B -band, which is shown in Figure 8. We compute

the TF residuals in velocity ($\log \sigma_{1d}$), not magnitude, to avoid biases caused by the magnitude limit. There is a weak relation between $U - B$ color and TF residual, with redder galaxies displaced to higher velocity, or equivalently lower B luminosity. The sense of the relation is such that measuring the TF relation in a redder bandpass, more closely related to stellar mass, will decrease the residual (cf. Kannappan et al. 2002). Highly obscured starbursts would have little effect on either M_B or line emission, though they might affect M_J . Unreddened starbursts that cause spuriously low linewidth of emission should be bluer and lie below the mean relation in σ_{1d} . Although there is a color-residual trend, it is weak and evolves little with redshift, so it cannot be the primary driver of TF evolution in magnitude, linewidth, or slope.

Figure 9 plots B -band TF residual as a function of HST/ACS half-light radius. This shows essentially no correlation of TF residual with R_{hl} , suggesting that TF evolution is not driven by compact galaxies alone.

Figure 10 plots B -band TF residual in $\log \sigma_{1d}$ as a function of the velocity to dispersion ratio V_{rot}/σ_{2d} , from the ROTCURVE fits to the 2-d spectra. Because the number of galaxies with ROTCURVE fits is smaller than the whole sample, we combine galaxies at all redshifts on the same plot, but we compute the TF residual from the fit appropriate to the galaxy's redshift. The triangles and open circles are rotation and dispersion dominated galaxies with $M_B < -18$ measured in well-aligned slits, as in the figures of Section 5 of Paper I. The filled circles and error bars are the mean of TF residual for the well-aligned-slit galaxies. There is a mild relation of residual with V_{rot}/σ_{2d} , in the sense that dispersion dominated galaxies are lower σ_{1d} for their magnitude.

We did not find evidence that this correlation with residual changes with redshift. Larger samples are needed to study redshift evolution of the resolved kinematics in any detail and to tell if evolution in the relative numbers of rotation and dispersion dominated galaxies could cause changes in the TF relation. The trend in TF residual is much smaller than the RMS scatter, indicating that the large scatter in the $\log \sigma_{1d}$ TF relation is not caused simply by mixing rotation and dispersion dominated galaxies. It does appear that the most rotation-dominated galaxies, with high V_{rot}/σ_{2d} , have smaller scatter about the TF in $\log \sigma_{1d}$. These are likely to be the galaxies with the most orderly kinematics.

5.1.3. Evolution in velocity or luminosity?

If the Tully-Fisher evolution is caused by an actual evolution in velocity or luminosity, which is the more likely suspect? A galaxy's luminosity can evolve substantially over an interval of several Gyr; we discuss luminosity evolution models in Section 6. The fact that our B and J Tully-Fisher relations evolve differently is a very strong argument that luminosity is evolving, since the aging of stellar populations causes a faster fading in B than in J .

We know that galaxies can change substantially in luminosity either through star formation episodes or fading, and that the blue galaxy population fades by ~ 1.3 mag per unit redshift (Wolf et al. 2003; Willmer et al. 2006), which is similar to the evolution we find in Tully-Fisher intercept in terms of magnitude. The locus of blue galaxies in color-magnitude space is consistent

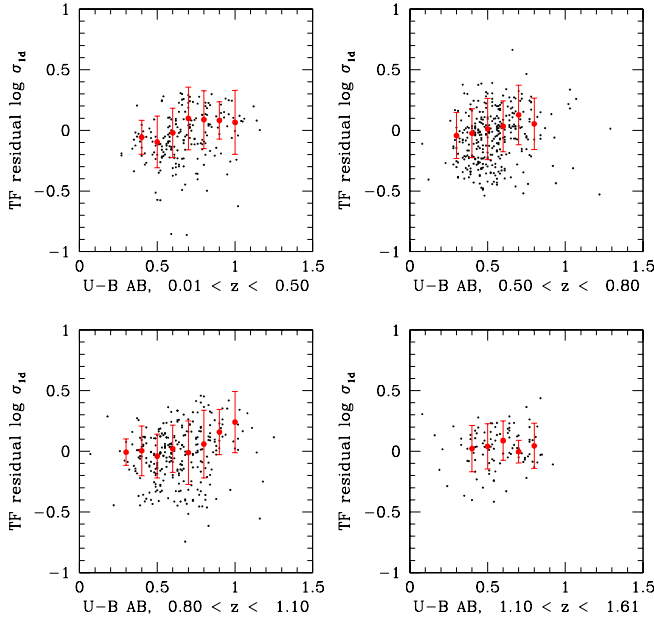


FIG. 8.— Tully-Fisher velocity residual as a function of $U - B$ restframe color, for galaxies with $M_B < -18$. There is a weak correlation between TF residual and color, with redder galaxies being at slightly higher velocity, hence slightly subluminal. The sense of this correlation is such that measuring the TF relation in a redder bandpass will decrease the residual. The weakness and lack of evolution in the color-residual correlation suggests that TF scatter and evolution are not driven by episodes such as extreme blue starbursts.

with this amount of quiescent evolution (Blanton 2005). Measurements of the luminosity-metallicity relation suggest differential luminosity evolution similar to what we found in the TF relation (Kobulnicky et al. 2003; Kobulnicky & Kewley 2004). A study of the luminosity-size relation in the TKRS/GOODS sample suggests that there is differential luminosity evolution as a function of radius with small galaxies fading more (Melbourne et al. 2006); differential changes could be a function of both radius and mass.

A galaxy’s characteristic velocity may also evolve with time. However, even in simplistic models, the relation between halo mass and velocity evolves so that the increase in velocity as mass increases with time is small (Mo, Mao & White 1998). Essentially this is because the universe is denser at earlier times. Simulations show that although halos are accreting mass as time goes on, the actual change in velocity dispersion is small at late times; this is especially true for blue galaxies, which are less likely to have undergone a recent major merger. A halo’s central density is established early when its mass accretion rate is high (Wechsler et al. 2002). As mass accretion slows, the characteristic central density begins to asymptote, and later mass accretion builds up the outer parts, so that the halo grows in outer radius, while the inner regions where we measure velocity change little.

A caveat is that because the inverse Tully-Fisher relation is shallow, small changes in velocity could still be significant. Nevertheless, our first step in modeling the TF

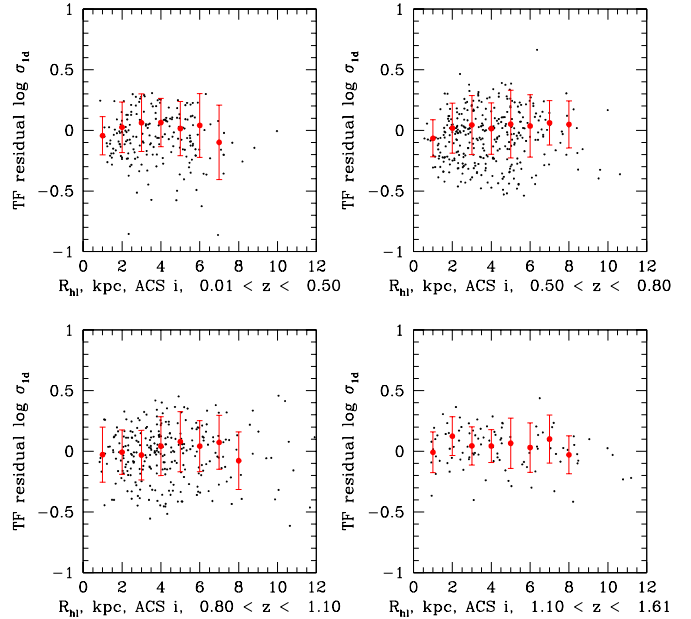


FIG. 9.— Tully-Fisher velocity residual as a function of half-light radius R_{hl} in ACS i , for galaxies with $M_B < -18$. There is at most a weak correlation between TF residual and radius, with larger galaxies being at slightly higher velocity, hence slightly subluminal. The correlation, if any, changes little with redshift.

evolution in Section 6 is the minimal model: we consider galaxies’ velocities as fixed and impose pure luminosity evolution models.

6. DISCUSSION: SIMPLE MODELS FOR TULLY-FISHER EVOLUTION

There does not yet exist a solid framework for predicting evolution in the Tully-Fisher relation from fully fledged models of galaxy evolution. Numerical models of disk galaxy formation have reproduced some of the properties of the local Tully-Fisher relation (e.g. Dalcanton, Spergel & Summers 1997; Mo et al. 1998) but using these to predict zeropoint and slope evolution has many degrees of freedom since the run of M/L with mass, and its change with time, is relatively adjustable.

Using N -body plus gas-dynamical simulations, Steinmetz & Navarro (1999) predicted a TF intercept evolution of ~ 0.7 mag from $z = 1$ to 0, but the evolution is highly dependent on the star formation recipe, and the simulations do not match the local intercept very well. Recently, Portinari & Sommer-Larsen (2006) have used simulations to predict TF intercept evolution of ~ 0.85 mag in B from $z = 1$ to 0, but very little evolution in the stellar mass TF intercept. The B -band intercept evolution is moderately less than we find, and the lack of stellar-mass intercept evolution agrees reasonably with our J -band measurements. However, they predict no slope evolution, which does not agree with our data. As in most N -body-derived models, their predicted low-redshift TF intercept is offset from the local data, and the disk scale-lengths are smaller than observed. Portinari & Sommer-Larsen correct for the latter, which appears not to be a major effect, but these differences indicate that

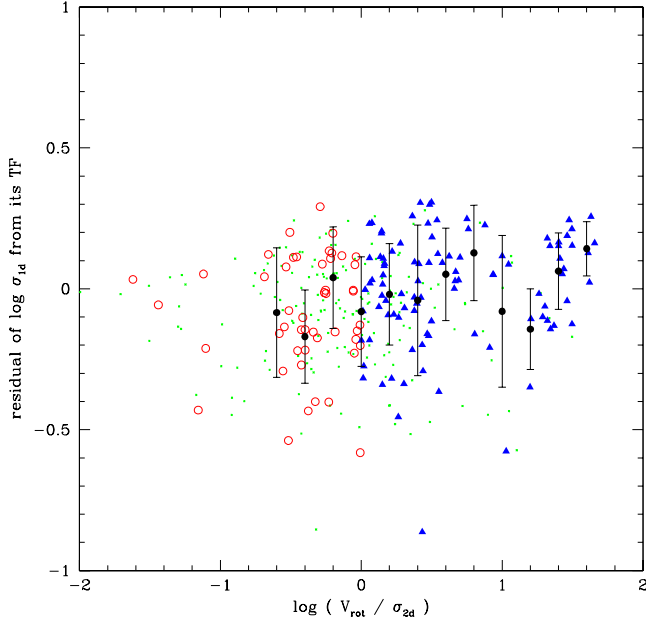


FIG. 10.— Tully-Fisher velocity residual in $\log \sigma_{1d}$ as a function of velocity/dispersion ratio measured in the 2-d spectra, $\log(V_{rot}/\sigma_{2d})$, for galaxies with $M_B < -18$. As in Paper I, rotation dominated galaxies are plotted as filled triangles, dispersion dominated galaxies are plotted as open circles, and round galaxies or those with misaligned slits are plotted as small Xes. The large points and errorbars are the mean and RMS of the aligned-slit galaxies. There is a mild relation between TF residual and V_{rot}/σ_{2d} .

it is still unclear how closely the evolution in N -body models can be related to that of real galaxies.

Here we consider some simplified models for Tully-Fisher evolution. A major utility of the Tully-Fisher relation is that it provides a way to link galaxies at different redshifts: based on luminosity and color alone, it is difficult to say what a blue galaxy at $z \sim 1$ will evolve into at low redshift (but see Blanton 2005 for a treatment of the population as a whole). By using the additional dimension of characteristic velocity, we can relate, in the mean, a high-redshift galaxy to its likely descendants. As a first simplification, as argued in Section 5, we suppose that the galaxies we are measuring evolve solely in luminosity and that a given galaxy’s characteristic velocity as measured by σ_{1d} changes little over our redshift range. We assume that our measured TF intercept and slope evolution are genuine, although the exact amounts are still uncertain, and ask if they can be explained reasonably, exploring the consequences of both intercept and slope evolution for simple models of galaxy histories.

6.1. Simple models: dwarfs and starbursting

6.1.1. Dwarfs: evolution at the faint end

One scenario that has been proposed is that the most active galaxies at moderate redshifts are low-mass, faint, or dwarfs, and that the strongest evolution should occur at the faint end of the Tully-Fisher relation. In this scenario, it is supposed that low-mass galaxies have had high star formation rates at redshifts < 1 while high

mass galaxies are already fairly evolved by then, or at any rate that more evolution happens in faint galaxies at $z < 1$ (e.g. Broadhurst, Ellis & Shanks 1988). Under this assumption, the luminosity evolution from $z \sim 1$ to now should be larger for low-mass galaxies. This predicts that at higher redshift, the inverse TF relation should be *steeper*.

Some intermediate- z Tully-Fisher measurements have suggested this sense of slope evolution, usually by detecting a small number of bright galaxies with low rotation velocities (e.g. Simard & Pritchet 1998; Böhm et al. 2004). As discussed above, local samples suggest that kinematic anomalies could be responsible for some low velocity measurements (Barton et al. 2001; Kannappan & Barton 2004). Further, the forward Tully-Fisher relation magnitude residuals at low velocity are skewed by the magnitude limit (see the Bamford et al. 2006 discussion of the Böhm sample), since overluminous low-velocity galaxies can be observed but underluminous ones are omitted from the samples. This and the inappropriate slopes produced by forward and bisector fits, discussed in Section 3.5, are arguments for analyzing the inverse TF relation, i.e. velocity residuals as a function of magnitude, as we do in this paper.

While the fast-evolving low-mass galaxy scenario sounds reasonable, in fact the fits of Section 3 show that the $z \sim 1$ inverse TF relations are marginally *shallower* than local. A steepened relation in which, for example, low-mass galaxies are 2 magnitudes brighter while high-mass galaxies are 1 mag brighter is definitively ruled out.

6.1.2. Bursts: intermittent luminosity evolution

Another possible scenario is that galaxies are intermittently brightened by bursts of star formation. Locally, galaxies with high star formation rates per unit mass tend to be low-mass (e.g. Brinchmann et al. 2004), but conceivably at higher redshifts, starbursting occurs in massive galaxies as well. However, it is not clear that plausible starbursts are large enough to move the most massive galaxies significantly (Barton et al. 2001). In a simple model of Tully-Fisher evolution driven by intermittent bursting, galaxies move to brighter luminosity when a burst happens, but remain at roughly constant (or slightly lower) linewidth, and then return to a baseline TF relation as the burst fades. To cause evolution, the bursts must be visible in B , rather than highly obscured starbursts.

This type of luminosity evolution driven by bursting has the desirable effect of predicting a shallower slope for the inverse Tully-Fisher relation at higher redshifts. Effectively, the galaxy distribution in $M_B - \log \sigma_{1d}$ space is broadened in M_B , so that fitting an inverse TF relation produces a shallower slope (although bursting does not explain why the slope evolution is similar in B and J).

However, if bursting is the major driver of TF evolution in the B band, the most overluminous galaxies should be the bluest in restframe color. This is not true in our sample. The color-magnitude relation for blue galaxies in Figure 3 of Paper I shows that even at $z = 1$, the brightest blue galaxies are also the reddest of the blue galaxies. The most luminous blue galaxies have restframe $U - B_{AB} \sim 0.7 - 0.8$, typical of a blue disk with moderate star formation rate, such as a local Sb-Sc. In Section 5.1.2 we argued that the fact that the B -band

TF evolution is strong for bright, *moderate-color* galaxies excludes a starburst effect on linewidths as the cause; it also excludes a starburst effect on magnitudes as the primary cause.

The weak relation of color and B -band Tully-Fisher residual shown in Figure 8 disfavors a bursting scenario. If the Tully-Fisher evolution were driven by more prevalent starbursts at higher redshift, the color-TF residual correlation should be stronger at higher redshift. Blue color and overluminosity (or low-velocity) should occur together, but Figure 8 shows that the color-TF residual is no stronger, and possibly weaker, at higher redshift. This is not to deny that starbursting happens or is more common at high redshift. Fluctuations in star formation rate could cause some of the scatter in the B -band TF relation. However, intermittent strong blue starbursts are not viable as the primary cause of Tully-Fisher slope evolution.

6.2. Models parametrized by star formation history

To make a more flexible and quantitative toy model, we calculate luminosity evolution from simple star formation histories. We assume that blue galaxies can be approximated by evolutionary tracks which build up stars over time, either through mass accretion or gas consumption, and use a family of models with exponentially declining star formation rates, “ τ -models” (Searle, Sargent & Bagnuolo 1973). These are parametrized by the SF timescale τ :

$$\text{SFR}(t) \propto \exp(-(t - t_f)/\tau), \quad (3)$$

where $t_f = t(z_f)$ is the cosmic time at the formation redshift z_f . For a model which forms stellar mass $M_{*,\text{tot}}$ as $t \rightarrow \infty$,

$$\text{SFR}(t) = \frac{M_{*,\text{tot}}}{\tau} \exp(-(t - t_f)/\tau), \quad (4)$$

$$M_*(t) = M_{*,\text{tot}}(1 - \exp(-(t - t_f)/\tau)). \quad (5)$$

Using τ -models, we make star formation timescale a function of galaxy mass. Models in which the star formation history depends on galaxy mass, specifically so that massive galaxies undergo vigorous star formation earlier than less-massive galaxies, have been much discussed recently under the rubric of “downsizing” (e.g. Cowie et al. 1996), although the idea is of very long standing (e.g. Tully, Mould & Aaronson 1982). Many studies have discussed the idea that SF timescale varies along the Hubble sequence, which is also essentially a mass sequence (e.g. Searle et al. 1973; Larson & Tinsley 1978).

We used the stellar evolutionary code PEGASE (Fiocc & Rocca-Volmerange 1997) to compute luminosity and color as a function of time for τ -models with a Kroupa IMF, solar metallicity, no stellar metallicity evolution, and with timescales $\tau = 0.1, 2, 4, 8, 10^4$ Gyr. The 0.1 Gyr model is effectively a single burst model appropriate for red galaxies, and the 10^4 Gyr model is effectively a constant star formation rate. No extinction or correction for dust content is applied. It is possible that evolving dust content affects the TF relation, although the trends of increasing metallicity and decreasing gas fraction with time could offset each other. Extinction must have less effect on the J -band TF relation than the B -band.

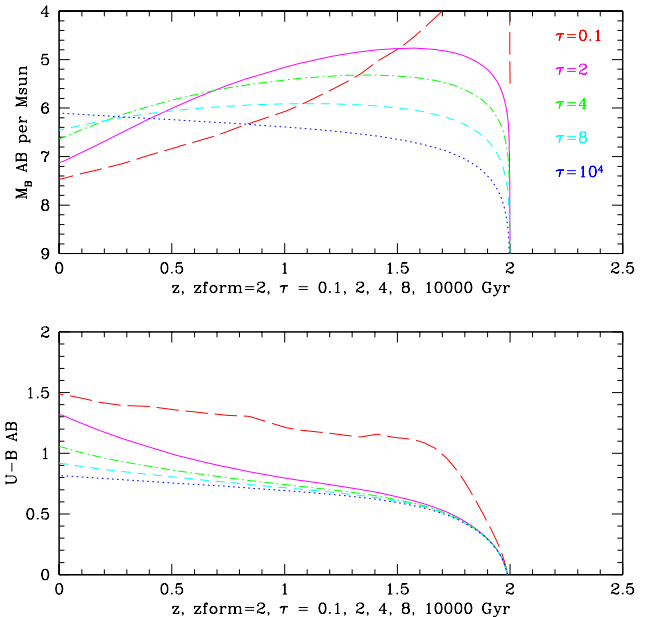


FIG. 11.— Magnitude and color evolution in M_B and $U - B$ of five τ -models with $\text{SFR} \propto \exp(-t/\tau)$. The models are started at $z_f = 2$, and have timescales $\tau = 0.1, 2, 4, 8, 10^4$ Gyr. The $\tau = 0.1$ model is effectively a single burst and the 10^4 model a constant SFR. The shorter-timescale models fade more from $z \sim 1$ to the present; the constant-SFR model gets brighter with time.

6.2.1. Differential magnitude evolution in τ -models

Figures 11 and 12 show tracks of these models in rest-frame magnitudes M_B and M_J (per unit total mass) and $U - B$ and $R - J$ colors, for $z_f = 2.0$. The $\tau = 0.1, 2, 4, 8$ Gyr models are normalized so that they form $1 M_\odot$ of stars as $t \rightarrow \infty$. By comparing two different redshifts in the upper panel of Figure 11, we can see how much a given model fades, and thus how it evolves in the Tully-Fisher relation.

The model track with $\tau = 2.0$ Gyr fades by ~ 1.2 mag in B from $z = 1.2$ to $z = 0.4$. Meanwhile, the model with $\tau = 8.0$ Gyr fades by only ~ 0.2 mag, and the constant star formation track actually increases in brightness. Similarly in J , the short- τ model fades by about 0.4 mag, while the longer timescale models brighten from $z = 1.2$ to $z = 0.4$. In retrospect, this behavior is easy to understand: short- τ models form a substantial amount of their stars at high redshift, before we have the chance to observe them, and these stars fade substantially from $z \sim 1$ to now. In contrast, long- τ models are still building up a large fraction of their stellar mass during the epochs we can observe, and fade little or even increase in luminosity.

The near-single-burst model becomes very red in $U - B$ quickly and evolves only gradually after that. The models with $\tau \geq 2$ Gyr stay blue for a long time, gradually moving redward, roughly consistent with color evolution in the observed blue galaxy population (Weiner et al. 2005; Blanton 2005). Toward lower redshift, the $\tau = 2$ Gyr model begins to peel away toward the red side of the color bimodality. However, because these are $U - B$

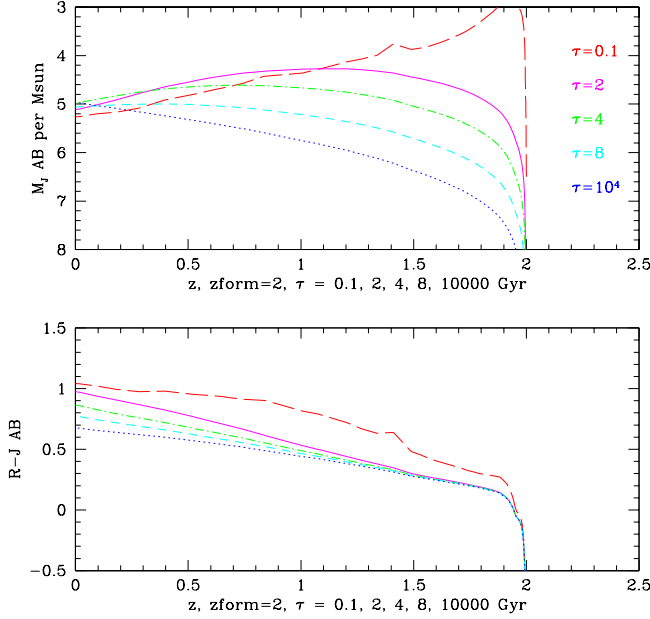


FIG. 12.— Magnitude and color evolution in M_J and $R - J$ of five τ -models with $SFR \propto \exp(-t/\tau)$. The models are started at $z_f = 2$, and have timescales $\tau = 0.1, 2, 4, 8, 10^4$ Gyr. The $\tau = 0.1$ model is effectively a single burst and the 10^4 model a constant SFR. The shorter-timescale models fade more from $z \sim 1$ to the present, while the longer timescale and constant-SFR models get brighter with time due to the buildup of stellar mass.

colors, even a small amount of additional late-time star formation would bluen the color significantly; predictions for $U - B$ color are less robust than predictions for B magnitude. The models only represent the galaxy population in the mean, as the real blue galaxy population has a color-magnitude relation with significant scatter in $U - B$ color (e.g. Figure 3 of Paper I).

In Section 3 we measured the linewidth Tully-Fisher relation in four redshift ranges with median redshift from $z = 0.4$ to 1.2. Thus we ask how the models evolve from $z = 1.2$ to 0.4. Figures 13 and 14 show how the τ -models fade and redden, for different choices of τ and formation redshift. The amount of fading in restframe B from $z = 1.2$ to 0.4 is a strong function of τ – apart from the single-burst $\tau = 0.1$ model, the short- τ models fade much more than the long- τ models. In contrast, the fading in B is not a strong function of redshift of formation z_f , unless z_f is pushed very close to the epoch of observation. However, the fading/brightening in J is more sensitive to z_f than are the measurements in B . In part this is because change in B measures relative change in the population of young stars at a given epoch, while change in J roughly measures change in the integrated stellar mass formed from z_f to the epoch of observation. In reasonable ranges of timescale and z_f , reddening in $U - B$ is not as strong a probe as fading.

To show how τ -models can predict Tully-Fisher evolution, we pinned each of the $\tau = \{2, 4, 8, 10^4\}$ Gyr tracks to the $z = 0.4$ B -band Tully-Fisher relation. We fixed $z_f = 2$ and assigned these values of τ to the magnitudes $M_B = \{-20, -19, -18, -17\}$ respectively, so that shorter

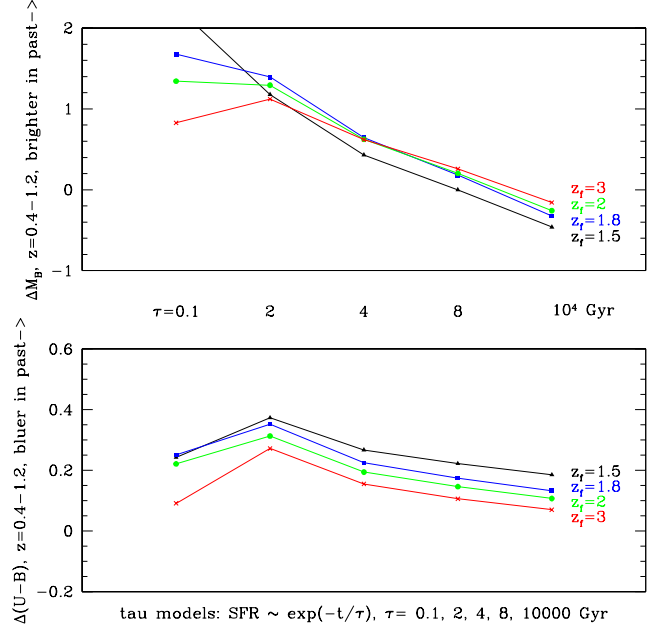


FIG. 13.— Magnitude fading and color reddening evolution in M_B and $U - B$ of the five τ -models, with timescales $\tau = 0.1, 2, 4, 8, 10^4$ Gyr. The upper panel shows magnitude fading in M_B from $z = 1.2$ to 0.4 as a function of timescale τ , with different tracks for formation redshifts from $z_f = 1.5$ to 3. The lower panel shows reddening in $U - B$ in the same manner. Fading and reddening are larger for shorter timescales (excepting the $\tau = 0.1$ single-burst model). The amount of fading is strongly dependent on timescale but only weakly dependent on formation redshift; observations of fading in B since $z = 1.2$ do not distinguish between $1.8 < z_f < 3$.

timescales belong to more luminous, hence more massive galaxies. Once z_f , τ , and magnitude at $z = 0.4$ are chosen, these parameters fix the normalization for each τ -model – effectively, the mass in stars+gas. The log σ_{1d} which corresponds to each τ comes from the $z = 0.4$ TF relation. Since we assume that log σ_{1d} does not change, the model tracks then give M_B at $z = 1.2$ and the high- z TF relation.

Table 2 gives the magnitudes and masses of the τ -models with $z_f = 2$ normalized to the $z = 0.4$ Tully-Fisher relation. Once each τ is assigned to a value of M_B at $z = 0.4$, log σ_{1d} is fixed by the Tully-Fisher fit, M_B at $z = 1.2$ is fixed by the past history of the τ -models, M_J at both epochs is fixed by the tracks of the τ -models, and the stellar masses are given by their M_*/L . For the $\tau = 2, 4, 8$ Gyr models, the total stellar+gas mass is given by integrating the SFR as $t \rightarrow \infty$. The $\tau = 10^4$ Gyr model does not converge to a reasonable amount, so we set it to have a plausible $M_*/M_{b,tot}$ at $z = 0$.

Table 3 gives the results of fitting “Tully-Fisher relations” to the four τ -models once they have been assigned values of M_B and log σ_{1d} at $z = 0.4$, by putting them on the observed TF relation at $M_B = \{-20, -19, -18, -17\}$. The B -band TF relation at $z = 0.4$ is the same as the observed relation by construction. The B TF relation at $z = 1.2$ and both J TF relations are determined by the tracks of the τ -models. The TF relation of the models is shallower at $z = 1.2$ in both B

TABLE 2
 τ MODELS NORMALIZED TO $z = 0.4$ B -BAND TF RELATION

τ , Gyr	M_B $z = 0.4$	M_B $z = 1.2$	M_J $z = 0.4$	M_J $z = 1.2$	$\log \sigma_{1d}$ (km s $^{-1}$)	$\log M_{b,tot}^a$ (M_\odot)	$\log M_*^b$ $z = 0.4$ (M_\odot)	$\log M_*^b$ $z = 1.2$ (M_\odot)	$\log \text{SFR}$ $z = 0.4$ (M_\odot/yr)	$\log \text{SFR}$ $z = 1.2$ (M_\odot/yr)
2	-20	-21.3	-21.6	-22.0	1.90	10.49	10.47	10.27	-0.11	0.80
4	-19	-19.6	-20.3	-20.2	1.74	9.99	9.88	9.55	-0.27	0.19
8	-18	-18.2	-19.1	-18.8	1.59	9.65	9.37	8.95	-0.58	-0.35
10^4	-17	-16.7	-18.0	-17.3	1.43	9.28	8.76	8.24	-0.92	-0.92

^aTotal stellar+gas mass of model

^bStellar mass formed by the given redshift

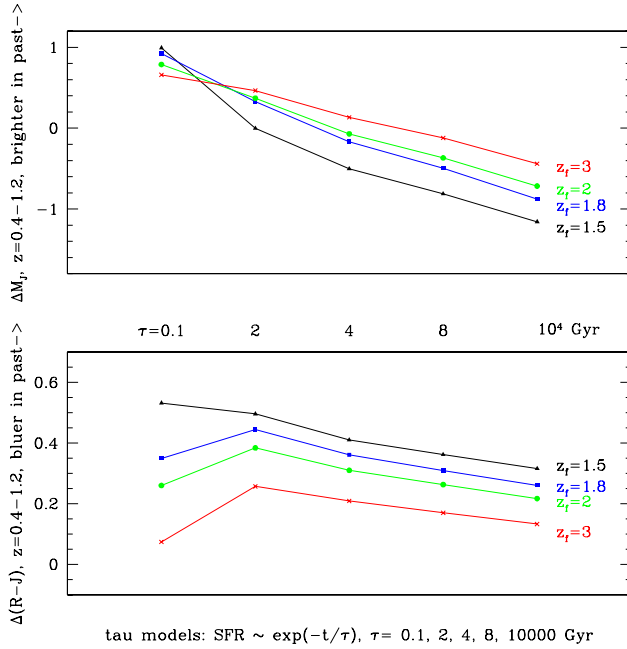


FIG. 14.— Magnitude fading and color reddening evolution in M_J and $R - J$ of the five τ -models, with timescales $\tau = 0.1, 2, 4, 8, 10^4$ Gyr. The upper panel shows magnitude fading in M_J from $z = 1.2$ to 0.4 as a function of timescale τ , with different tracks for formation redshifts from $z_f = 1.5$ to 3 . The lower panel shows reddening in $R - J$ in the same manner. Fading and reddening are larger for shorter timescales (excepting the $\tau = 0.1$ Gyr single-burst model). The amounts of fading and reddening are fairly strongly dependent on timescale, and more sensitive to formation redshift than are M_B and $U - B$.

and J ; the intercept evolution is much less in J than in B .

Figure 15 shows the model TF relations compared to the TF data in B . The short-dashed line shows our $z = 0.4$ TF relation from Figure 1, and the τ -models which are pinned to it are plotted as filled circles. Rather than plot all the galaxies, we show the weighted means of the $0 < z < 0.5$ data in magnitude bins, as open circles; the error bars are the standard error of the mean. (The weighted means are higher than the fit line because higher $\log \sigma_{1d}$ points have smaller observational errors, as discussed in Section 3.2.1.) The τ -models at $z = 1.2$ are plotted as filled triangles, and the long-dashed line is

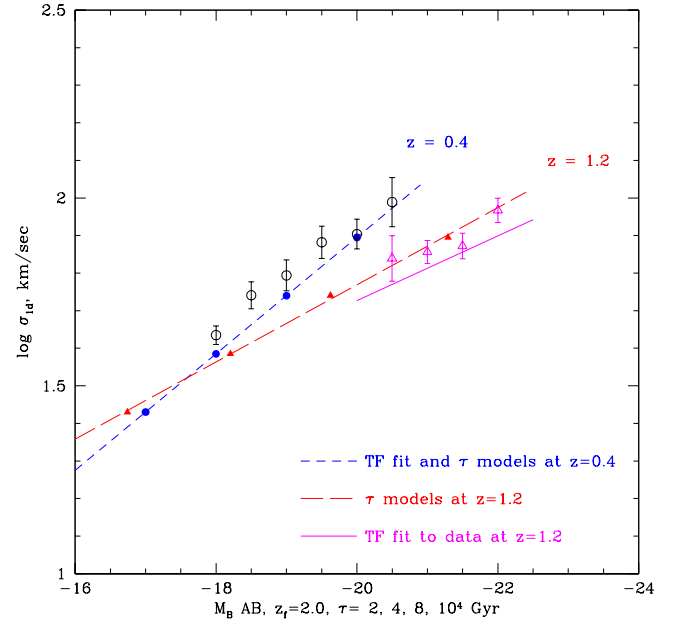


FIG. 15.— B -band Tully-Fisher evolution predictions from τ models. Four models with $z_f = 2$ and $\tau = 2, 4, 8, 10^4$ Gyr (filled circles) are placed on the $z = 0.4$ Tully-Fisher relation (short-dashed line). The open circles are the $0 < z < 0.5$ linewidth data weighted means binned by magnitude, and the error bars are standard error of the mean. Data fainter than $M_B = -18$ are not used in the TF fit and are omitted. The τ models are evolved back to $z = 1.2$, assuming that $\log \sigma_{1d}$ does not change and only M_B evolves. The $z = 1.2$ models and a linear fit to them are plotted as filled triangles and long-dashed line, showing the luminosity and slope evolution. The $z = 1.2$ models continue to lie on a linear TF relation, although this was not forced by any constraint. The $1.1 < z < 1.61$ linewidth data binned by magnitude are plotted as open triangles, and the TF fit at $1.1 < z < 1.61$ is plotted as a solid line.

a fit to their $\log \sigma_{1d}$ on M_B . The solid line is the TF relation fit to the galaxies at $1.1 < z < 1.61$, and the open triangles are the $1.1 < z < 1.61$ data in bins of magnitude. The models produce a high- z B -band TF relation that is shifted and shallower than at low redshift, as is seen in the data.

Figure 16 shows the analogous comparison between models and TF data in J . Once the set of models is normalized to the $z = 0.4$ TF relation in B -band, all the

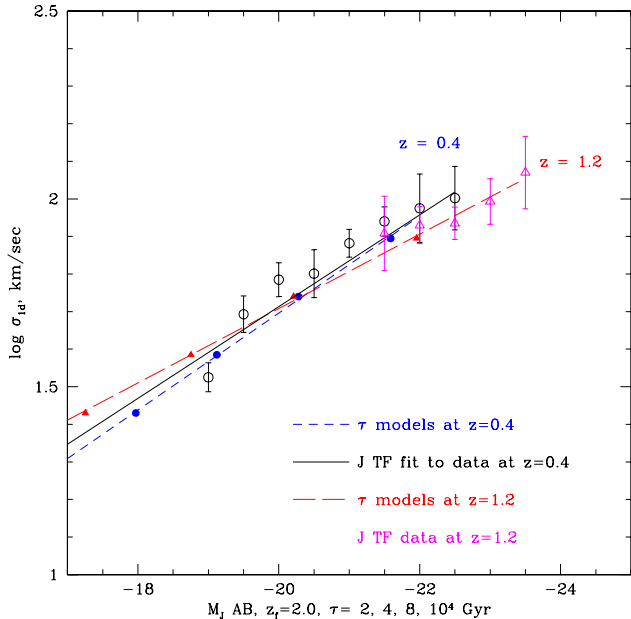


FIG. 16.— J -band Tully-Fisher evolution predictions from τ models. Four models with $z_f = 2$ and $\tau = 2, 4, 8, 10^4$ Gyr were placed on the $z = 0.4$ B -band Tully-Fisher relation. Their position in J is then fixed by the models (filled circles). The open circles are the $0 < z < 0.5$ linewidth data weighted means binned by J magnitude, and the error bars are standard error of the mean. Data fainter than $M_J = -19$ are not used in the TF fit and are omitted. The τ models are evolved back to $z = 1.2$, assuming that $\log \sigma_{1d}$ does not change and only M_J evolves. The $z = 1.2$ models and a linear fit to them are plotted as filled triangles and long-dashed line, showing the luminosity and slope evolution. The $z = 1.2$ models continue to lie on a linear TF relation, although this was not forced by any constraint. The $1.1 < z < 1.5$ linewidth data binned by J magnitude are plotted as open triangles.

TABLE 3
EVOLUTION IN TF RELATION PREDICTED BY A SET OF τ MODELS

Band	Redshift	Zeropoint (mag)	Intercept A dex	Slope B dex/mag
B	$z = 0.4$	-21	2.050 ^a	-0.155 ^a
B	$z = 1.2$	-21	1.872	-0.103
J	$z = 0.4$	-22	1.954	-0.129
J	$z = 1.2$	-22	1.906	-0.099

^aFixed to the observed $z = 0.4$ B -band TF relation by construction.

degrees of freedom are used up: the $z = 0.4$ relation between linewidth and J magnitude is fixed by the model colors. The $z = 0.4$ model TF relation comes out linear and agrees quite well with the actual relation, which is encouraging, though it mostly means that the models have the correct relation of $B-J$ color to mass at $z = 0.4$. The models at $z = 1.2$ produce a J -band TF relation that is only slightly shifted in intercept, and is shallower than at low redshift. Essentially the “pivot point,” where the low and high redshift TF relations cross, is at higher mass (shorter τ) in J than in B -band.

The τ -models produce a magnitude evolution only slightly less than indicated by the high-redshift data and TF fit. Of course, we had a degree of freedom in picking the normalization of τ to B magnitude at $z = 0.4$, but the SFR timescales, colors and stellar mass fractions implied are reasonable. Thus the amount of Tully-Fisher intercept evolution is consistent with pure luminosity evolution and very reasonable star formation histories and colors. The τ -models also preserve the linearity of the TF relations: at $z = 1.2$ they lie on a near-perfect line, though in principle they could have produced a nonlinear relation. This required no fine-tuning, and again shows that the persistence of a linear TF relation is consistent with a reasonable variation of SF history with mass.

The critical feature of using τ -models, with τ a function of magnitude or velocity, is that they naturally produce differential fading, and pinning them along the low-redshift TF relation produces a slope that will evolve with redshift. Figure 15 shows that our normalization of τ -models to magnitude at $z = 0.4$, which gives close to the correct luminosity evolution, also produces slope evolution that agrees with the data.

These τ -models are not at all the only plausible set of star formation histories, and do not include metallicity or dust evolution; observationally, there is still uncertainty in the high-redshift Tully-Fisher slope, due to both small numbers and the limited magnitude range at high redshift. We do not claim that the models are in any way unique. However, Figures 15 and 16 show that reasonable models for star formation history as a function of mass naturally produce evolution in the Tully-Fisher ridgeline intercept and slope that matches both optical and near-IR observations.

The τ -models also predict a color-magnitude relation and its evolution, although here metallicity evolution and dust require more careful treatment (Tully et al. 1982). The differential evolution in luminosity and dependence of τ on luminosity are generally consistent with models derived from evolution in the luminosity-metallicity relation (Kobulnicky et al. 2003; Kobulnicky & Kewley 2004). Ultimately, realistic models should be constrained by evolution in the velocity-magnitude-color relations. The models must also reproduce the scatter in these relations. Our simplistic τ -models predict color and TF relations with no scatter; in addition to metallicity and dust, it is almost certain that episodic variation about the smooth star-formation history produces some of the scatter (e.g. Larson & Tinsley 1978).

6.2.2. Differential star formation rate evolution

Because the high mass galaxies have the shortest SFR timescales while low mass galaxies build up stars at a more nearly constant rate, our simple model predicts that the $\sim 10\times$ higher global star formation rate at $z \sim 1$ compared to local (e.g. Lilly et al. 1996) is dominated by higher SFR in *massive* galaxies, rather than low-mass objects. Our τ -models from high to low mass have SFRs which are $\{1.6, 0.8, 0.4, 0\}$ dex greater at $z = 1$ than $z = 0$, for $\tau = \{2, 4, 8, 10^4\}$ Gyr. These are roughly compatible with the observed drop in SFR, although a full prediction of the evolution of the global SF rate requires a convolution with the luminosity or mass function. This scenario agrees with $z = 0.5-1$ observations of IR-luminous galaxies that show a high SFR in luminous

spirals (Bell et al. 2005; Melbourne, Koo & Le Floch 2005).

One interesting prediction of a model that makes SFR timescale a function of mass is that the slope of SFR on mass should vary with redshift. The low-mass galaxies with constant SFR evolve slowly, but the high-mass galaxies are at much higher SFR at high redshift than now. Figure 17 plots the evolution of our set of τ -models in specific SFR (SFR/stellar mass) versus stellar mass. The models are started at $z_f = 2$ and normalized to fit the $z = 0.4$ B -band TF relation as in the previous section. Each set of connected points represents the mean specific SFR-stellar mass relation at redshifts from 1.5 to 0. The models predict substantial change in slope of this relation. However, the details of this relation depend on the redshifts of formation. The labels in the rightmost column show the effect of starting the models at $z_f = 3$; the models reach a given evolutionary state at higher z . Increasing z_f can push back the epoch at which massive galaxies have high SFR, making them hard to observe, and any real relation will have a large scatter. If one pushes to high enough redshift, massive galaxies may have multiple progenitors, violating our assumption that a single track corresponds to a single object. However, it is hard to avoid the general trend that high-mass objects or their progenitors form relatively more stars at early times, in order to become older and redder by the present day.

Measurements of SFR as a function of stellar mass ought to show a change in slope. Unfortunately, the limited depth of mid-infrared surveys makes slope change difficult to see in $24 \mu\text{m}$ selected samples (e.g. Bell et al. 2005). There is considerable scatter in any observed SFR–stellar mass relation, and selection effects tend to eliminate the low-mass and low-SFR objects at high redshift, making it hard to measure an unbiased mean relation. Surveys of SFR from the [O II] line have tended to show a trend of SFR(mass) that does not evolve in slope, but rather an overall decrease in intensity with time (e.g. Brinchmann et al. 1998; Bauer et al. 2005). However, SFRs from [O II] uncorrected for extinction may have selection effects and biases that are correlated with mass and change with redshift. Nevertheless, at some point, the SFR(mass) slope must change with time, or it is very difficult to explain the blue galaxy color-magnitude relation.

7. CONCLUSIONS

We measured line-of-sight integrated kinematic linewidths σ_{1d} and spatially resolved line-of-sight rotation V_{rot} and dispersion σ_{2d} from the galaxy spectra of the Team Keck survey of the GOODS-N field. In Paper I we showed that linewidths are a measure of internal kinematics that is relatively robust against observational effects, although there is significant scatter between any individual galaxy linewidth and true circular velocity or dynamical mass. We use 968 linewidths of galaxies with $M_B < -18$ and 677 linewidths of galaxies with $M_J < -19$ to measure evolution of the restframe B and J -band Tully-Fisher relations from $z \sim 0.4$ to 1.2. This is the largest sample of high-redshift galaxies with kinematics to date, and samples the blue galaxy population without morphological or other pre-selection. It allows both an internal comparison, without having

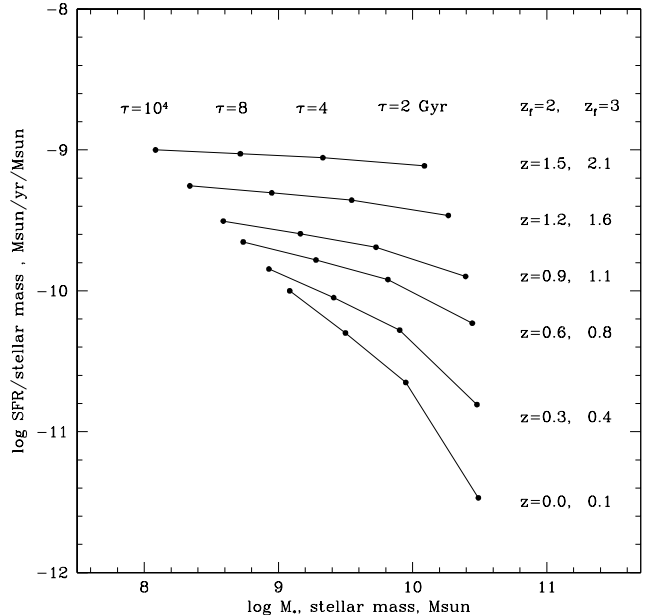


FIG. 17.— An example prediction from τ -models of the evolution of the relation of specific star formation rate, SFR/stellar mass, versus stellar mass. The τ -models were started at $z_f = 2$ and normalized to fit the $z = 0.4$ B -band TF relation. Each set of points connected by a line represents the specific SFR–stellar mass relation as a function of τ at a given redshift, labeled in the column of redshifts under “ $z_f = 2$.” Because high mass galaxies have shorter SFR timescales, they fall more quickly in specific SFR. The rightmost column of redshifts, under “ $z_f = 3$,” shows where the models fall for the same time gaps but a formation redshift of 3. If the models are started earlier, the low-redshift behavior is similar but the epoch where high-mass galaxies have high specific SFR is pushed back.

to fix to a local TF relation, and the measurement of intercept and slope evolution.

The intrinsic scatter in the Tully-Fisher relation for linewidths is large, 0.18 dex in $\log \sigma_{1d}$, which requires special care in fitting methods; we derive a maximum likelihood fitting method in the Appendix. The intrinsic scatter is partly due to the lack of inclination and extinction corrections; kinematic peculiarity is likely to both contribute to the scatter and to reduce its non-gaussianity by reducing the number of orderly low-inclination objects with low observed velocity. Correlations of TF residual with other parameters are weak and do not suggest obvious second-parameter sources of scatter or evolution.

In the B -band linewidth TF relation, there is very significant intercept evolution and 3σ evidence for slope evolution. The sense of the slope evolution is such that the high-redshift inverse TF relation, velocity as a function of magnitude, $V(M)$, is shallower than at low redshift. The J -band linewidth TF relation shows relatively little evolution in intercept, but a similar evolution in slope to that found in B -band. The B -band TF relation for rotation velocities V_{rot} also supports intercept evolution, but the sample is too small and noisy to measure slope evolution.

The sense of slope evolution is most easily interpreted

as differential luminosity evolution: the most luminous galaxies at $z > 1$ fade by more than the less luminous galaxies. There is more fading in B than in J band. In the mean, a galaxy with $M_B = -21.5$ at $z = 1.2$ fades by ~ 1.5 B magnitudes to $z = 0.4$, but only by ~ 0.5 mag in J . The B -band evolution is larger than some previous TF measurements; some differences are that our sample has many more galaxies at high redshift, that it is not morphologically selected to favor normal disks, and that it does not reject galaxies with non-rotating kinematics. Because the evolution is differential, the amount of fading seen is also dependent on the magnitudes of the different TF samples. The fading of $1 - 1.5$ mag in B at fixed velocity that we see is similar to the fading of 1.3 ± 0.3 mag in L_B^* in the blue galaxy LF measured by Willmer et al. (2006), and the fading of luminosity at fixed radius seen by Melbourne et al. (2006). A simple, but not unique, model for these results is that most of the blue galaxy population evolves unaltered by merging or density evolution since $z \sim 1$, with stellar population fading the primary driver of luminosity evolution.

We present a simplistic model to explain differential luminosity evolution: we construct galaxy histories with star formation rate declining exponentially with time (τ -models, $\text{SFR} \propto e^{-t/\tau}$), and make the SFR timescale τ a function of mass along the Tully-Fisher relation. In this scenario, massive galaxies have short τ and form the bulk of their stars early, before $z = 1$, while low mass galaxies have long τ and build up stellar mass slowly. This arrangement of τ -models has long been indicated by the color-magnitude relation for blue galaxies (e.g. Tully et al. 1982). The model correctly predicts that the massive galaxies fade substantially from $z \sim 1$ to now, while low mass galaxies fade little since they are still building stellar mass. The decrease of the global SFR since $z \sim 1$ is thus dominated by the decrease in SFR in massive galaxies, while the activity of low-mass galaxies changes relatively little in the mean. Thus the Tully-Fisher slope

evolution, as differential luminosity evolution, is a natural outcome of an appealing model for star formation histories of blue galaxies.

Measurements of Tully-Fisher evolution help us to constrain models of galaxy evolution by relating galaxies at one epoch to another, tracking the evolutionary descent of galaxies. In this paper we have taken the simplest approach of assuming pure luminosity evolution, i.e. that galaxies' characteristic velocities evolve much less than their luminosities, and that the blue galaxy population is essentially constant in number. Future work on this subject can be more sophisticated. Theoretical ideas about the evolution of velocity with halo mass can improve this approach. The color-magnitude relation, infrared magnitudes, stellar mass estimates, and the luminosity and velocity functions provide a wealth of data which models must confront. The scatter about these relations should be related to episodic variations about the mean star formation histories. Together these may be used to understand the mass assembly history of galaxies.

We dedicate this paper to the memory of Bob Schommer. We thank the TKRS, GOODS, and Hawaii groups for making their catalogs and data publicly available. We thank Greg Novak for helpful discussions on least-squares fitting. BJW has been supported by grant NSF AST-0242860 to S. Veilleux. The TKRS was supported by NSF grant AST-0331730 and this project has been supported by NSF grant AST-0071198 to UCSC. AJM acknowledges support from NSF grant AST-0302153 through the NSF Astronomy and Astrophysics Postdoctoral Fellows Program. The authors wish to recognize and acknowledge the cultural role and reverence that the summit of Mauna Kea has always had within the indigenous Hawaiian community. We are most fortunate to have the opportunity to conduct observations from this mountain.

REFERENCES

- Abraham, R.G., van den Bergh, S., Glazebrook, K., Ellis, R.S., Santiago, B.X., Surma, P., & Griffiths, R.E. 1996, *ApJS*, 107, 1
- Akritas, M.G., & Bershadsky, M.A. 1996, *ApJ*, 470, 706
- Bamford, S.P., Milvang-Jensen, B., Aragón-Salamanca, A., & Simard, L. 2005, *MNRAS*, 361, 109
- Bamford, S.P., Aragón-Salamanca, A., & Milvang-Jensen, B. 2006, *MNRAS*, 366, 308
- Barton, E.J., Geller, M.J., Bromley, B.C., van Zee, L., & Kenyon, S.J. 2001, *AJ*, 121, 625
- Bauer, A.E., Drory, N., Hill, G.J., & Feulner, G. 2005, *ApJ*, 621, L89
- Bell, E. F., et al. 2005, *ApJ*, 625, 23
- Bell, E. F., Wolf, C., Meisenheimer, K., Rix, H.-W., Borch, A., Dye, S., Kleinheinrich, M., & McIntosh, D. H. 2004, *ApJ*, 608, 752
- Blanton, M.R. 2005, *ApJ*, submitted, astro-ph/0512127
- Böhm, A., et al. 2004, *A&A*, 420, 97
- Brinchmann, J., et al. 1998, *ApJ*, 499, 112
- Brinchmann, J., Charlot, S., White, S.D.M., Tremonti, C., Kauffmann, G., Heckman, T., & Brinkmann, J. 2004, *MNRAS*, 351, 1151
- Broadhurst, T.J., Ellis, R.S., & Shanks, T. 1988, *MNRAS*, 235, 827
- Capak, P., et al. 2004, *AJ*, 127, 180
- Conselice, C.J., Bundy, K., Ellis, R.S., Brinchmann, J., Vogt, N.P., & Phillips, A.C. 2005, *ApJ*, 628, 160
- Cooper, M.C. et al. 2006, *MNRAS* in press, astro-ph/0603177
- Cowie, L.L., Songaila, A., Hu, E.M., & Cohen, J.G. 1996, *AJ*, 112, 839
- d'Agostini, G. 2005, preprint physics/0511182
- Dalcanton, J.J., Spergel, D.N., & Summers, F.J. 1997, *ApJ*, 482, 659
- Faber, S.M. et al. 2006, *ApJ*, submitted, astro-ph/0506044
- Fioc, M., & Rocca-Volmerange, B. 1997, *A&A*, 326, 950
- Flores, H., Hammer, F., Puech, M., Amram, P. & Balkowski, C. 2006, *A&A*, in press, astro-ph/0603563
- Forbes, D.A., Phillips, A.C., Koo, D.C., & Illingworth, G.D. 1996, *ApJ*, 462, 89
- Fouque, P., Bottinelli, L., Gouguenheim, L., & Paturel, G. 1990, *ApJ*, 349, 1
- Giavalisco, M., et al. 2004, *ApJ*, 600, L93
- Giovanelli, R., Haynes, M.P., Herter, T., Vogt, N.P., da Costa, L.N., Freudling, W., Salzer, J.J., & Wegner, G. 1997, *AJ*, 113, 53
- Gull, S. F. 1989, in *Maximum Entropy and Bayesian Methods*, ed. J. Skilling (Dordrecht: Kluwer), 511
- Isobe, T., Feigelson, E.D., Akritas, M.G., & Babu, G.J. 1990, *ApJ*, 364, 104
- Kannappan, S.J., & Barton, E.J. 2004, *AJ*, 127, 2694

- Kannappan, S.J., Fabricant, D.G., & Franx, M. 2002, AJ, 123, 2358
- Kobulnicky, H.A., & Gebhardt, K. 2000, AJ, 119, 1608
- Kobulnicky, H.A., & Kewley, L.J. 2004, ApJ, 617, 240
- Kobulnicky, H.A., et al. 2003, ApJ, 599, 1006
- Larson, R.B., & Tinsley, B.M. 1978, ApJ, 219, 46
- Lilly, S.J., Le Fevre, O., Hammer, F., & Crampton, D. 1996, ApJ, 460, L1
- Mallén-Ornelas, G., Lilly, S.J., Crampton, D., & Schade, D. 1999, ApJ, 518, L83
- Melbourne, J., Koo, D.C., & Le Floch, E. 2005, ApJ, 632, L65
- Melbourne, J., Phillips, A.C., Harker, J., Novak, G., Koo, D.C., & Faber, S.M. 2006, ApJ, submitted
- Metevier, A.J., Koo, D.C., Simard, L., & Phillips, A.C. 2006, ApJ, 643, 764
- Milvang-Jensen, B., Aragón-Salamanca, A., Hau, G.K.T., Jørgensen, I., & Hjorth, J. 2003, MNRAS, 339, L1
- Mo, H.J., Mao, S., & White, S.D.M. 1998, MNRAS, 295, 319
- Nakamura, O., Aragón-Salamanca, A., Milvang-Jensen, B., Arimoto, N., Ikuta, C., & Bamford, S.P. 2006, MNRAS, 366, 144
- Novak, G.S., Faber, S.M., & Dekel, A. 2006, ApJ, 637, 96
- Pisano, D.J., Kobulnicky, H.A., Guzmán, R., Gallego, J., & Bershady, M.A. 2001, AJ, 122, 1194
- Pizagno, J. et al. 2005, ApJ, 633, 844
- Portinari, L., & Sommer-Larsen, J. 2006, astro-ph/0606531
- Press, W.H., Flannery, B.P., Teukolsky, S.A. & Vetterling, W.T. 1992, Numerical Recipes, (Cambridge: Cambridge U.P.)
- Reichart, D.E. 2001, ApJ, 553, 235
- Rix, H., Guhathakurta, P., Colless, M., & Ing, K. 1997, MNRAS, 285, 779
- Sakai, S. et al. 2000, ApJ, 529, 698
- Schechter, P.L. 1980, AJ, 85, 801
- Searle, L., Sargent, W.L.W., & Bagnuolo, W.G. 1973, ApJ, 179, 427
- Simard, L., & Pritchett, C.J. 1998, ApJ, 505, 96
- Steinmetz, M., & Navarro, J.F. 1999, ApJ, 513, 555
- Teerikorpi, P. 1987, A&A, 173, 39
- Tremaine, S., et al. 2002, ApJ, 574, 740
- Tully, R.B., Mould, J.R., & Aaronson, M. 1982, ApJ, 257, 527
- Tully, R.B. & Pierce, M.J. 2000, ApJ, 533, 744
- Tully, R.B., Pierce, M.J., Huang, J., Saunders, W., Verheijen, M.A.W., & Witchalls, P.L. 1998, AJ, 115, 2264
- Vogt, N.P., et al. 1996, ApJ, 465, L15
- Vogt, N.P., et al. 1997, ApJ, 479, L121
- Vogt, N.P. 2000, ASP Conf. Ser. 197: Dynamics of Galaxies: from the Early Universe to the Present, 197, 435
- Watanabe, M., Yasuda, N., Itoh, N., Ichikawa, T., & Yanagisawa, K. 2001, ApJ, 555, 215
- Wechsler, R.H., Bullock, J.S., Primack, J.R., Kravtsov, A.V., & Dekel, A. 2002, ApJ, 568, 52
- Weiner, B.J., et al. 2005, ApJ, 620, 595
- Weiner, B.J., et al. 2006, ApJ, (Paper I)
- Willick, J.A. 1994, ApJS, 92, 1
- Willick, J.A. 1999, ApJ, 516, 47
- Willmer, C.N.A., et al. 2006, ApJ, in press
- Wirth, G.D., et al. 2004, AJ, 127, 3121
- Wolf, C., Meisenheimer, K., Rix, H.-W., Borch, A., Dye, S., & Kleinheinrich, M. 2003, A&A, 401, 73
- Ziegler, B.L., et al. 2002, ApJ, 564, L69

APPENDIX

MAXIMUM LIKELIHOOD FITTING OF DATA WITH INTRINSIC SCATTER

There are a number of approaches to fitting straight lines to data with errors in both coordinates, and a perhaps surprising lack of consensus on the “best” method (see e.g. Akritas & Bershady 1996; Gull 1989; Isobe et al. 1990; Tremaine et al. 2002; Novak et al. 2006). This problem becomes more acute when the data have significant intrinsic scatter beyond the observational errors. Fitting such data with a model that does not account for intrinsic scatter will generally yield biased fits. Recent approaches to fitting with intrinsic scatter are outlined by Akritas & Bershady (1996) and Novak et al. (2006). Here we derive a maximum likelihood with scatter (MLS) method; a maximum likelihood approach was also used by Willick (1999). For similarly motivated approaches from general Bayesian considerations, see Reichart (2001) and d’Agostini (2005); the latter derives a formula very similar to ours.

Suppose a model with a linear relationship in (x, y) with ridgeline $y_{pred} = A + Bx$ and gaussian intrinsic scatter S_y in the y -coordinate, where the scatter is assumed to be independent of x .¹² The probability density distribution of objects drawn from this model is:

$$P_{mod}(x, y) = \frac{1}{\sqrt{2\pi}S_y} \exp\left(-\frac{(y - y_{pred})^2}{2S_y^2}\right) \times P_{dist}(x) \quad (\text{A1})$$

$P_{dist}(x)$ is the probability density of x -values of the population; it could be used to express the limits of the distribution or selection limits in x . For the basic model without selection limits we will simplify by taking a uniform $P_{dist}(x) = 1$. Nonlinear relations $y_{pred}(x)$ can also be accommodated.

Note that, for linear $y_{pred}(x)$, the model distribution has a gaussian cross-section in x as well as in y . In fact we could substitute $x_{pred} = \alpha + \beta y$, with $\alpha = -A/B$, $\beta = 1/B$, and $S_x = S_y/B$ to obtain the same functional form with x and y exchanged, and a prefactor of β that normalizes the probability density. Either way one writes the distribution, it represents a set of parallel contours of probability: a ridgeline with probability decreasing away from the ridge. Thus, for a uniform $P_{dist}(x)$ and no selection limits, there is nothing about this parametrization which makes a distinction between scatter in x and in y . Rather, choosing whether to assign scatter to x or y changes the covariance among the intercept, slope and scatter parameters; one computes probability in a different 3-space, $P(A, B, S_y)$ or $P(\alpha, \beta, S_x)$. In practice, one should assign the scatter to the variable which does not have strong selection limits, e.g. velocity in the Tully-Fisher application.

For a set of observations x_i, y_i , with errors e_{xi}, e_{yi} , each observation represents a probability density distribution $P_{obs,i}(x, y)$. The simplest form for the $P_{obs,i}$ is an elliptical gaussian with independent errors, but this formalism can accommodate covariant and non-gaussian errors. In a Bayesian sense, the probability of the model given the data is

¹² The scatter could be made a function of x or y at the expense of more model parameters and a significant decrease in elegance.

given by an application of Bayes's Theorem, convolving the model distribution with the probability of each data point and the prior probability of the parameters:

$$P(A, B, S_y | x_i, y_i) \propto P_{prior}(A, B, S_y) \times \prod_i (P_{mod} \circ P_{obs,i}), \quad (\text{A2})$$

where $P_{mod} \circ P_{obs,i} = \int \int dx dy P_{mod}(x, y) P_{obs,i}(x, y)$. If we don't have any preconceptions about the parameters we can use a uniform $P_{prior} = 1$. The best-fit parameters can be found by maximizing the conditional probability $P(A, B, S_y | x_i, y_i)$ over the parameter space of (A, B, S_y) . It is convenient to work with $L(A, B, S_y) = \ln P(A, B, S_y | x_i, y_i)$. If (1) the model has gaussian scatter S_y , (2) the measurement errors are independent in x and y , making the $P_{obs,i}$ elliptical gaussians, and (3) there are no selection effects that limit the region over which we can integrate the convolution, L has a very convenient closed form:

$$L = -\Sigma \frac{(y_i - (A + Bx_i))^2}{(B^2 e_{xi}^2 + e_{yi}^2 + S_y^2)} + \text{constant}. \quad (\text{A3})$$

Equation A3 is immediately recognizable as a generalization of the χ^2 minimization least-squares fitting formula of Press et al. (1992), by adding the intrinsic scatter S_y in quadrature to the y -error e_{yi} . This method (GLS) has been used in astronomy by Tremaine et al. (2002), Pizagno et al. (2005), and tested by Novak et al. (2006); these authors determine the value of S_y by requiring that total $\chi^2/N = 1$. The present derivation advances the GLS formula by giving it a firmer statistical justification, making the assumptions more transparent, and demonstrating that the choice of whether to add the scatter in x or y is not *ad hoc*, but encodes a choice about the covariance of the parameters. Using the GLS formula is effectively accepting both the assumptions made by the MLS method and the assumptions we made above to derive Equation A3. A Fortran program, `mlsfit.f`, which performs the MLS fit over a grid of parameters using either Equation A3 or the Gaussian form of the convolution of Equation A2, and which can be modified for other convolutions, is available from the authors.

A useful property of this derivation is that integrating the probability density convolution in Equation A2, rather than using Equation A3, easily accomodates non-gaussian scatter, or arbitrary error distributions including non-gaussian and covariant errors. Additionally it can be used to fit over more suitable variables; in the body of this paper we use the velocity dispersion (see also Equation 1):

$$y = \log \sigma_{1d} = \log \left(\frac{c}{\lambda_{obs}} \sqrt{\sigma_{obs}^2 - \sigma_{inst}^2} \right). \quad (\text{A4})$$

This equation is ill-behaved for kinematically poorly resolved galaxies, when σ_{obs} is close to or less than σ_{inst} . By changing variables and integrating Equation A2 over σ_{obs} , the formalism handles these galaxies without numerical singularities, although the intrinsic Tully-Fisher scatter becomes non-Gaussian in σ_{obs} and the convolution integrals become computationally expensive.

We can also compute the probability $P(A, B, S_y | x_i, y_i)$ over a grid of parameters and use this to find the *expectation value* of the parameters, which is potentially more meaningful than the location of maximum likelihood (peak conditional probability). However, the two are very close for well constrained models with gaussian scatter and errors. Computing $P(A, B, S_y | x_i, y_i)$ also allows us to compute confidence intervals by finding contours of probability in the parameter space, or e.g. the interval of A, B , or S_y that contains 68% of the probability. These confidence intervals allow estimates of the error on parameters A, B , and S_y . Using the extended least-squares method allows an estimate of the error on scatter S_y through the change in χ^2 at the best-fit (A, B) (Novak et al. 2006), but this method does not generalize easily to complex contours of probability. (However, the value of the intrinsic scatter S_y is, as always, sensitive to the accuracy of the error estimates on individual measurements, and usually less robust than the best fit A and B .)

For the Tully-Fisher application in the present paper, the sample is subject to magnitude limits, so assumption (3) above is violated. This could lead to incompleteness bias, but our simulations discussed in Section 3.5 show that the effect is negligible for this sample, because the range of the data in magnitude is much larger than the magnitude errors. However, the selection limits and the shallow slope of the inverse TF relation $V(M)$ dictate that we should add the intrinsic scatter in velocity, not in magnitude.